Monotonic and cyclic tests on Kaolin - a database for the development, calibration and verification of constitutive models for cohesive soils with focus to cyclic loading

T. Wichtmann[i], Th. Triantafyllidis[ii]

Abstract: A database with about 60 undrained monotonic and cyclic triaxial tests on Kaolin is presented. In the monotonic tests the influences of consolidation pressure, overconsolidation ratio, displacement rate and sample cutting direction have been studied. In the cyclic tests the stress amplitude, the initial stress ratio and the control (stress vs. strain cycles) have been additionally varied. Isotropic consolidation lead to a failure due to large strain amplitudes with eight-shaped effective stress paths in the final phase of the cyclic tests, while a failure due to an excessive accumulation of axial strain and lens-shaped effective stress paths were observed in the case of anisotropic consolidation with $q^{\mathrm{ampl}} < |q^{\mathrm{av}}|$. The rate of pore pressure accumulation grew with increasing amplitude and void ratio (i.e. decreasing consolidation pressure and overconsolidation ratio). The "cyclic flow rule" well-known for sand has been confirmed also for Kaolin: With increasing value of the average stress ratio $|\eta^{\mathrm{av}}| = |q^{\mathrm{av}}|/p^{\mathrm{av}}$ the accumulation of deviatoric strain becomes predominant over the accumulation of pore water pressure. The tests on the samples cut out either horizontally or vertically revealed a significant effect of anisotropy. In the cyclic tests the two kinds of samples exhibited an opposite inclination of the effective stress path. Furthermore, the horizontal samples showed a higher stiffness and could sustain a much larger number of cycles to failure. All data of the present study are available from the homepage of the first author. They may serve for the examination, calibration or improvement of constitutive models dedicated to cohesive soils under cyclic loading, or for the development of new models.

Keywords: Kaolin, triaxial tests, undrained conditions, monotonic loading, cyclic loading, database

1 Introduction

For numerical studies of the behaviour of geotechnical structures (e.g. foundations, damns, embankments) on water-saturated cohesive soils subjected to cyclic loading (e.g. caused by wind or waves in case of coastal or off-shore structures, by traffic in case of infrastructure or by shear wave propagation during earthquakes) the application of sophisticated constitutive models for the soil is indispensable. Such models have to be developed and calibrated based on high-quality cyclic laboratory tests with manifold boundary conditions, so that they can be checked for as many different cases as possible. Such close examination of the constitutive equations based on element tests creates confidence for an application of the model to different real problems. Amongst others, the constitutive model should adequately describe the effective stress path with the relaxation of effective mean stress (pore pressure accumulation) and the stress-strain relationship with the increase in the strain amplitude and the development of cumulative deviatoric strains during a cyclic loading applied under undrained conditions.

Data from cyclic tests on cohesive soils suitable for the development or calibration of constitutive models are rare in the literature. A necessary criterion for an element test is a rather low strain rate, leading to a homogeneous field of pore water pressure within the samples. Furthermore, beside choosing too large loading frequencies (e.g. 0.1 Hz as typical for offshore conditions), most studies in the liter-

ature were restricted to a rather small amount of tests with a limited bandwidth of boundary conditions (e.g. triaxial tests with isotropic consolidation and stress cycles). Therefore, there is a need for a comprehensive database with results from undrained cyclic laboratory tests with varying boundary conditions and load characteristics performed on a cohesive soil.

Such database has been collected from triaxial tests on Kaolin at the Institute of Soil and Rock Mechanics (IBF) at KIT during the last few years. It comprises tests on samples consolidated either isotropically or anisotropically and subjected to stress or strain cycles. The consolidation stress (mean pressure p_0 and stress ratio $\eta_0 = q_0/p_0$), the stress or strain amplitude, the overconsolidation ratio, the strain rate and the orientation of the samples (conventional vertical or horizontal cutting direction) have been varied. The loading has been applied slow enough to guarantee a homogeneous field of pore pressure within the samples. Beside the cyclic tests, monotonic triaxial and oedometric tests have been additionally performed to complete the database. It is currently in use for the development of constitutive models at the IBF, but it is the intention of this paper to make the data public also for external use. For that purpose, analogously to an existing database for fine sand [130, 131], the experimental data collected from all tests on Kaolin are made available on the homepage of the first author [125]. In case of the cyclic tests, the data provided at [125] contain both the measured data versus time and selected quantities versus the number of cycles.

---

[i] Research Assistant, Institute of Soil Mechanics and Rock Mechanics (IBF), Karlsruhe Institute of Technology (KIT), Germany (corresponding author). Email: torsten.wichtmann@kit.edu

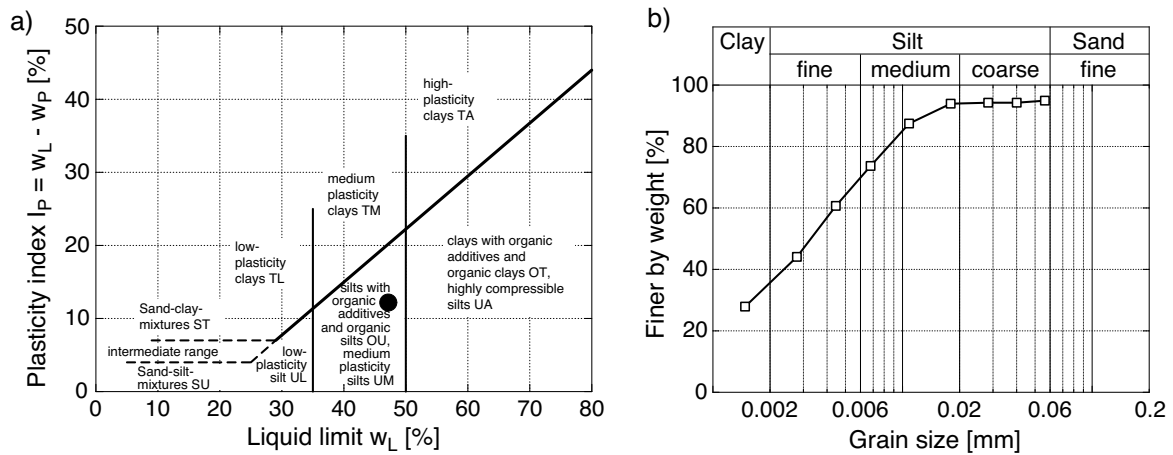[ii] Professor and Director of the IBF, KIT, Germany

Fig. 1: a) Position of the tested Kaolin in the Casagrande diagram, b) grain size distribution curve from a sedimentation analysis

Fig. 2: Preparation of reconstituted triaxial samples of Kaolin via slurry consolidation

2 Test material, specimen preparation and testing procedure

The Kaolin used in the present study has been purchased in dry powder form from the company "Gebrüder Dorfner GmbH & Co. Kaolin- und Kristallquarzsand-Werke KG" in Hirschau, Germany (product name "Kaolin K1 gemahlen"). From index tests a liquid limit $w_L = 47.2$ % and a plastic limit $w_P = 35.0$ % have been determined, resulting in a plasticity index $I_P = 12.2$ %. Lying below the A-line in Casagrande's I_P-w_L diagram (Figure 1a) this soil is classified as medium-plastic silt (in contrast to some finer Kaolin clays tested in the literature). The grain size distribution curve obtained from a sedimentation analysis is provided in Figure 1b. The grain density of the test material is $\varrho_s = 2.675$ g/cm^3.

The samples were consolidated out of a slurry having a water content of $w/w_L = 2.5$. For that purpose dry Kaolin powder was mixed with demineralized water under vacuum for at least 12 hours. The slurry was pre-consolidated in a plexiglas cylinder (Figure 2). The axial loading during this pre-consolidation was applied pneumatically. The maximum vertical stress during pre-consolidation was 100 kPa in all tests. The pre-consolidated samples had a diameter of $d = 130$ mm and a height of $h \approx 130$ mm.

Afterwards triaxial samples ($d = h = 50$ mm) were cut out of the centre of the pre-consolidated Kaolin sample.

Samples with $d = h = 50$ mm (i.e. a height-to-diameter ratio $h/d = 1$) are the standard for testing of cohesive soils at the IBF, because the deformations of these samples are more uniform and the consolidation and homogenization of pore water pressure within the sample take less time than in case of samples with $d = 50$ mm and $h = 100$ mm (i.e. $h/d = 2$). In an earlier study performed by the first author on a soft marine Norwegian clay [126] samples with $h/d = 1$ and $h/d = 2$ were found to deliver almost identical results under undrained cyclic loading conditions.

For the sample preparation a split mould lined by a latex membrane and equipped with a cutting tool at its bottom was used (Figure 2). The pre-consolidated Kaolin was carefully pressed out of the pre-consolidation cylinder into the cutting tool and thus into the mould. The excessive Kaolin outside the cutting edge was removed. The inner side of the rubber membrane was smeared with a thin layer of grease in order to reduce friction between membrane and the Kaolin raising inside the mould. When the Kaolin had exceeded the top of the mould by at least 30 mm, the surface of the sample was planed (Figure 2). The triaxial sample was separated from the rest of the pre-consolidated material by inserting a steel sheet below the cutting edge. Then the mould was rotated by 180°, the cutting tool was removed and the other end of the sample was planed. Finally, the sample was mounted into the triaxial device. Smeared end
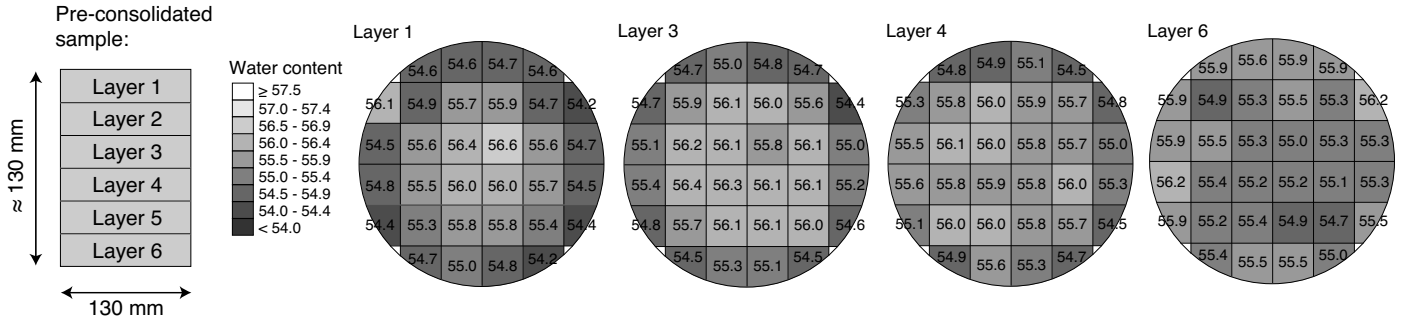
Fig. 3: *Distribution of water content in a pre-consolidated Kaolin sample*

plates (thin layer of grease + rubber disc) with a small central porous stone (diameter 10 mm) were used.

Some preliminary tests on the homogeneity of the pre-consolidated samples have been performed. For that purpose several pre-consolidated samples were not used for triaxial tests, but cut into approx. 200 cubes. Based on the water contents determined for each of these cubes the distribution of w in the pre-consolidated sample was found quite homogeneous, in particular in the central part where the triaxial samples are taken (see Figure 3).

In the triaxial device all samples were water-saturated with a back pressure of 500 kPa and consolidated step-wise to the initial stress of the test. In case of anisotropic consolidation stresses, first an isotropic consolidation to a mean effective stress $p = \sigma'_{30}$ was undertaken, with σ'_{30} being the initial effective lateral stress. Afterwards the axial stress was stepwise increased or decreased to the target value σ'_{10} of the test. After consolidation under the final effective stress the drainage was closed and the monotonic (Section 3) or cyclic (Section 4) loading was started.

3 Tests with monotonic loading

The programme of the triaxial tests with monotonic loading is summarized in Table 1. In a first series of tests the samples were isotropically consolidated to five different effective mean pressures $p_0 = 50, 100, 200, 300$ and 400 kPa. The undrained monotonic shearing was applied with a displacement rate $\dot{s} = 0.025$ mm/min (corresponds to a strain rate of about $\dot{\varepsilon}_1 = 0.05$ %/min). The measured development of deviatoric stress $q = \sigma'_1 - \sigma'_3$ with axial strain ε_1 and the effective stress paths in the p-q-plane with $p = (\sigma'_1 + 2\sigma'_3)/3$ are given in Figure 4a,b. With the exception of the final phase of the tests the material response is contractive. The failure envelope shown as dashed curve in the p-q-plane in Figure 4b is further used in the analysis of the cyclic test data for comparison purpose. The failure surface shows a distinct curvature in the p-q plane, similar as reported e.g. in [11, 19].

The rate dependence of the undrained monotonic response of Kaolin is rather weak. This is confirmed by the results of four undrained monotonic triaxial tests on normally consolidated samples presented in Figure 4c,d. Displacement rates between $\dot{s} = 0.005$ mm/min and 0.25 mm/min (corresponding to strain rates of about 0.01 %/min $\leq \dot{\varepsilon}_1 \leq 0.5$ %/min) have been tested. As expected, with increasing strain rate the material response renders slightly less contractive and the undrained shear strength moderately increases. Stronger strain rate effects

Series	Test	p_0 [kPa]	OCR [-]	h_0 [mm]	e_0 [-]	$\dot{s}$ [mm/min]	Cutting direction
1	M1	50	1.33*)	49.8	1.434	0.025	vertical
	M2	100	1	49.4	1.332		
	M3	200		48.2	1.332		
	M4	300		47.6	1.244		
	M5	400		46.8	1.214		
2	M6	200	1	47.9	1.124	0.005	vertical
	M7			47.9	1.177	0.025	
	M8			48.6	1.140	0.05	
	M9			48.3	1.111	0.25	
3	M10	100	2	48.6	1.223	0.025	vertical
	M11		4	47.7	1.083		
	M12		8	47.3	1.009		
4	M13	100	1	49.0	1.226	0.025	vertical
	M14			46.9	1.174		vertical
	M15			48.2	1.165		horizontal

Table 1: Programme of undrained monotonic triaxial tests. Initial void ratios e_0 and initial sample heights h_0 have been measured at the consolidation mean stress p_0 prior to shearing. (*) $OCR = p_{\max}/p_0$ has been calculated with the maximum effective mean stress during pre-consolidation $p_{\max} = (100 + 2 \cdot 50)/3 = 66.7$ kPa, applying an estimated lateral stress $\sigma'_3 = 0.5\sigma'_1 = 50$ kPa)

are usually observed for materials with higher plasticity (e.g. [2, 3, 26, 35, 45, 48, 66, 73, 90, 94, 107, 111, 116, 117]).

The diagrams in Figure 4e,f demonstrate the effect of overconsolidation on the stress-strain relationships and the effective stress paths. After being built into the triaxial device, the samples were subjected to a drained isotropic preloading towards $p_{\max} = 200, 400$ or 800 kPa, followed by a drained unloading to $p_0 = 100$ kPa, resulting in overconsolidation ratios of $OCR = p_{\max}/p_0 = 2$, 4 and 8. The higher OCR, the lower is the void ratio e_0 at p_0 prior to the undrained monotonic shearing. Consequently, with increasing OCR the material response is rendered more dilative and higher deviatoric stresses, i.e. larger undrained monotonic strengths are reached. The effective stress paths measured for the higher OCR values are bounded by the failure envelope encountered in the monotonic tests on normally consolidated samples (Figure 4b). A similar effect of overconsolidation on dilatancy or on the effective stress paths, respectively, is documented in [32, 91, 97, 100, 107, 110, 118, 133]. The increase in the undrained strength with increasing OCR is consistent with [23, 29, 61, 62, 91].
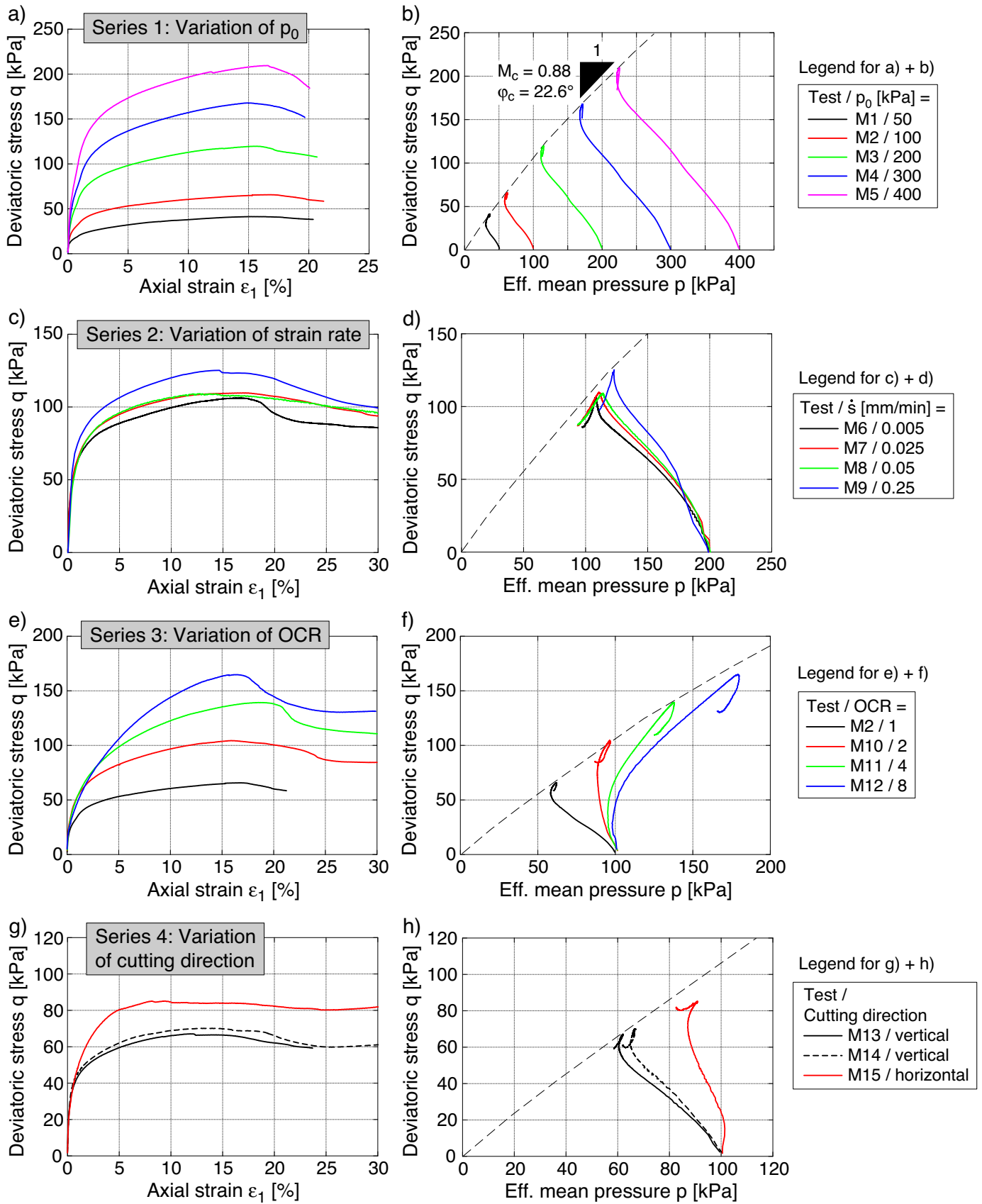
Fig. 4: *Stress-strain relationships and effective stress paths measured in undrained monotonic triaxial tests on Kaolin samples with different a),b) initial mean pressures p_0, c),d) displacement rates $\dot{s}$, e),f) overconsolidation ratios OCR, g),h) cutting directions of the samples*

The results of the tests presented in Figure 4g,h demonstrate a distinct effect of the inherent anisotropy. The samples were either cut out conventionally in the vertical direction ($\alpha = 0°$, α = angle between sedimentation and loading direction) or in the horizontal direction ($\alpha = 90°$). In order to gather a horizontally oriented triaxial specimen from the pre-consolidated cylinders, a cuboidal sample has been cut out first which was encased by a plexiglas cube. This cube has been rotated by 90° before the samples have been prepared in the same way as shown in Figure 2. It is evident in Figure 4g,h that the sample cut out in the horizontal direction ($\alpha = 90°$) shows a more dilative response and a higher undrained shear strength than those taken vertically ($\alpha = 0°$). This is in accordance with [98] but in contrast to several other studies in the literature that reported about a more contractive behaviour and an accompanying decrease of the undrained shear strength s_u with increasing α [2,47,71,72,82,83,102,109]. Summarizing earlier studies, [28] concluded that s_u may either increase or decrease with α, depending on the type of clay.

Some additional oedometric tests with either stress or strain control have been also performed. The samples have not been pre-consolidated, but the Kaolin was mixed at a water content slightly above the liquid limit, before being smeared into the oedometer ring. Figure 5 presents the measured curves of void ratio versus axial stress. In the stress-controlled test several creep, unloading and reloading phases have been inserted (Figure 5a). The $e(\sigma_1)$ curves from the strain-controlled tests with different strain rates (Figure 5b) confirm the relatively low rate dependence already concluded from the triaxial tests.

4 Tests with cyclic loading

In several test series the overconsolidation ratio OCR, the initial mean pressure p_0, the initial stress ratio $\eta_0 = q_0/p_0$, the stress amplitude q^{ampl} and the displacement rate $\dot{s}$ have been varied. The testing programme is listed in Table 2. The cyclic loading was applied with a constant displacement rate $\dot{s}$. In order to test a certain stress amplitude q^{ampl}, the loading direction was changed once the specified minimum or maximum values of deviatoric stress were reached (pseudo stress-control). The cyclic loading was stopped when a certain value of axial strain (failure criterion, usually $|\varepsilon_1| = 10\%$) was reached.

4.1 Variation of stress amplitude at isotropic consolidation stresses

Eight tests with different stress amplitudes in the range 30 kPa $\leq q^{\mathrm{ampl}} \leq$ 70 kPa were performed (tests C1-C8 in Table 2). Two amplitudes (45 and 50 kPa) were tested twice in order to check repeatability. All samples were consolidated isotropically at $p_0 = 200$ kPa in the triaxial device. The cyclic loading was applied with a displacement rate $\dot{s}$ = 0.1 mm/min.

Typical results from test C6 with $q^{\mathrm{ampl}} = 50$ kPa are given in Figure 6. Figure 6a shows the increase in pore water pressure u and the accompanying decrease of the axial and lateral effective stress components, σ_1' and σ_3', respectively, with increasing number of cycles. In contrast to sand (see e.g. [130,131]) a state with zero effective stress is not reached in these tests on Kaolin with isotropic consolidation. The continuous increase in the axial strain amplitude with N is evident in Figure 6b. Due to the progressive
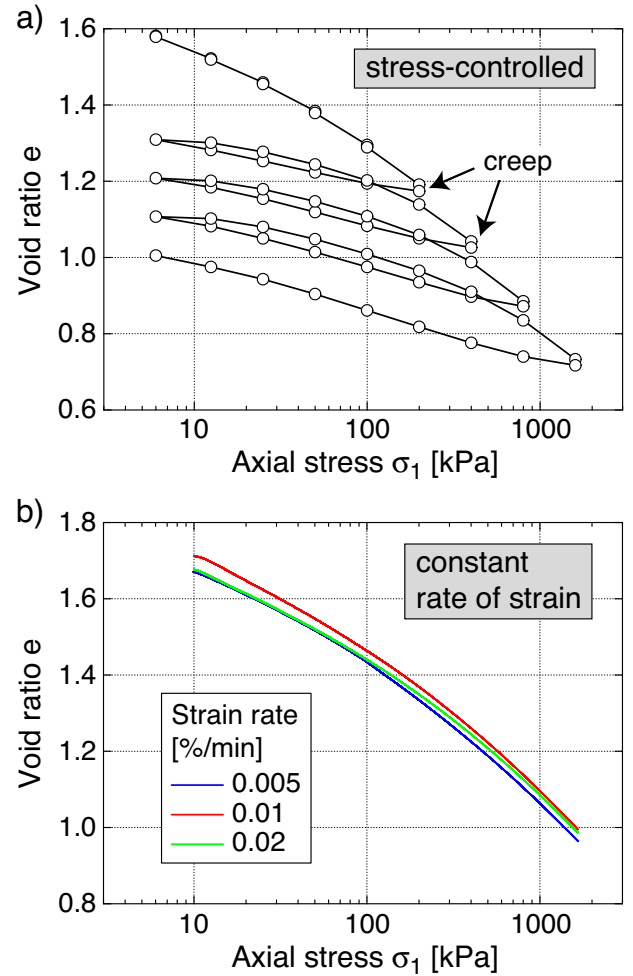

Fig. 5: *Void ratio versus axial stress from oedometric tests with a) stress control or b) constant rate of strain*

decrease of stiffness and the constant displacement rate, the time period T of the individual cycles gets larger with increasing duration of a test. The resulting stress-strain curves provided in a q-ε_1 diagram in Figure 6c enclose a much larger area than typically observed for sand [130,131], that means the material damping is much higher for the tested Kaolin. Furthermore, in contrast to typical results for sand, the stress-strain curves during the final phases of the test do not run along the p-axis (i.e. at $q \approx 0$). The effective stress path in the p-q plane obtained from this test is given in Figure 7b. The stress loop during the final stage of the test (last one to two cycles) is highlighted in black colour, while the rest of the path is formatted in grey. With the exception of the final stage of the test the effective stress path is significantly inclined towards the left upper corner of the p-q diagram. In the final stage it passes an eight-shaped loop, not reaching $p = q = 0$. The orientation of the path during that stage is marked by arrows in Figure 7b.

The effective stress paths measured in two other tests with lower ($q^{\mathrm{ampl}} = 40$ kPa) or higher ($q^{\mathrm{ampl}} = 60$ kPa) stress amplitudes, respectively, are shown in Figure 7a,c (tests C2 and C7 in Table 2). These stress paths look similar to that of test C6 with the intermediate stress amplitude $q^{\mathrm{ampl}} = 50$ kPa. The same applies to the stress-strain hys-

Test series	Variation of	Test	OCR [-]	h_0 [mm]	e_0 [-]	p_0 [kPa]	η_0 [-]	q_0 [kPa]	q^{ampl} [kPa]	ζ [-]	$\varepsilon_1^{\mathrm{ampl}}$ [%]	$\dot{s}$ [mm/min]	N_f [-]
1	q^{ampl} ($\eta_0 = 0$)	C1	1	47.4	1.250	200	0	0	30	0.15	-	0.1	>4368
		C2		46.7	1.147				40	0.2			492
		C3		46.3	1.224				45	0.225			242
		C4		46.7	1.193				45	0.225			131
		C5		46.7	1.145				50	0.25			68
		C6		46.6	1.252				50	0.25			35
		C7		46.4	1.202				60	0.3			11
		C8		46.3	1.121				70	0.35			7
2	$\dot{s}$ (Series 1)	C9	1	47.0	1.143	200	0	0	45	0.225	-	0.01	81
		C10		46.9	1.272							0.02	58
		C11		47.8	1.294							0.05	51
		C12		46.7	1.221							0.5	109
3	$\dot{s}$ (Series 2)	C13	1	46.8	1.293	200	0	0	50	0.25	-	0.01	24
		C14		46.9	1.228							0.05	40
		C15		47.1	1.298							0.5	26
4	p_0	C16	1.33*)	49.7	1.397	50	0	0	10	0.2	-	0.1	526
		C17	1.0	48.9	1.410	75			15				138
		C18		47.4	1.244	100			20				368
		C19		48.6	1.295	125			25				94
		C20		48.3	1.272	150			30				131
		C21		47.1	1.112	250			50				995
		C22		46.4	1.143	300			60				983
5	η_0 (Compression)	C23	1	43.5	1.206	200	0.625	125	30	0.15	-	0.1	5
		C24		44.2	1.212		0.5	100					29
		C25		45.9	1.200		0.375	75					131
		C26		46.6	1.249		0.25	50					319
		C27		46.9	1.319		0.125	25					>2272
6	η_0 (Extension)	C28	1	47.3	1.248	200	-0.125	-25	30	0.15	-	0.1	>7286
		C29		47.3	1.248		-0.25	-50					>2418
		C30		49.3	1.229		-0.375	-75					>1790
		C31		49.2	1.180		-0.5	-100					163
7	q^{ampl} ($\eta_0 = 0.375$)	C32	1	46.6	1.142	200	0.375	75	15	0.075	-	0.1	>10000
		C33		45.8	1.239				20	0.1			1176
		C34		45.4	1.283				25	0.125			426
		C35		45.7	1.251				35	0.175			19
		C36		46.2	1.227				40	0.2			19
8	OCR	C37	1.5	48.6	1.239	100	0	0	30	0.3	-	0.1	116
		C38	2	48.1	1.200								531
		C39	2.5	48.2	1.146								904
9	Cut-out horizontally	C40	1	50.0	1.125	200	0	0	45	0.225	-	0.1	1359
		C41		49.6	1.252				45	0.225			614
		C42		48.5	1.100		0.5	100	30	0.15			2721
10	Strain cycles	C43	1	46.0	1.046	300	0	0	-	-	1	0.1	-
		C44		47.8	1.057						2		
		C45		46.4	1.035						5		

Table 2: Programme of undrained cyclic triaxial tests. Initial void ratios e_0 and initial sample heights h_0 have been measured at the consolidation mean stress p_0 prior to the start of the cycles. Amplitude-pressure ratio is defined as $\zeta = q^{\mathrm{ampl}}/p_0$. (*) See remarks in the caption of Table 1)
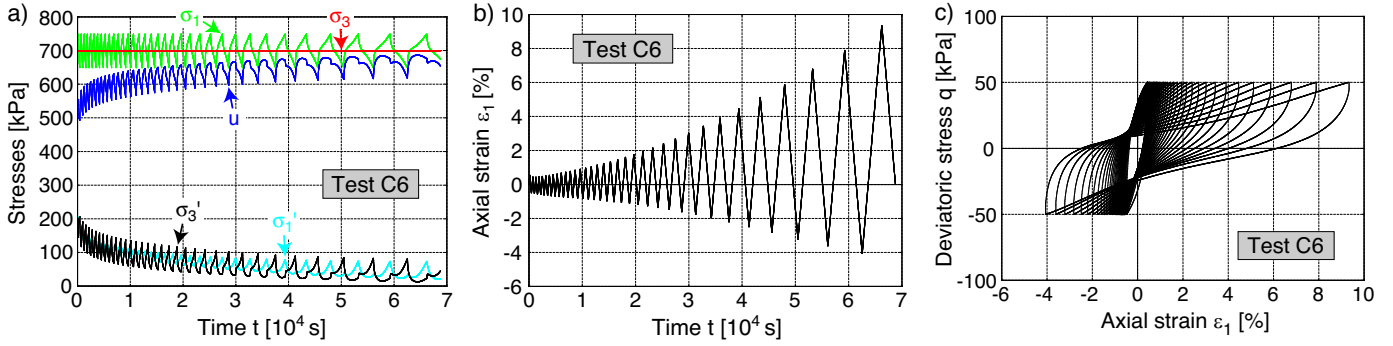
Fig. 6: Typical results of an undrained cyclic test with isotropic consolidation (test C6 in Table 2 with $OCR = 1$, $p_0 = 200$ kPa, $\eta_0 = 0$, $q^{\mathrm{ampl}} = 50$ kPa, $\dot{s} = 0.1$ mm/min): a) Total or effective stress components and pore water pressure as a function of time t, b) Axial strain ε_1 as a function of time t, c) Deviatoric stress q versus axial strain ε_1
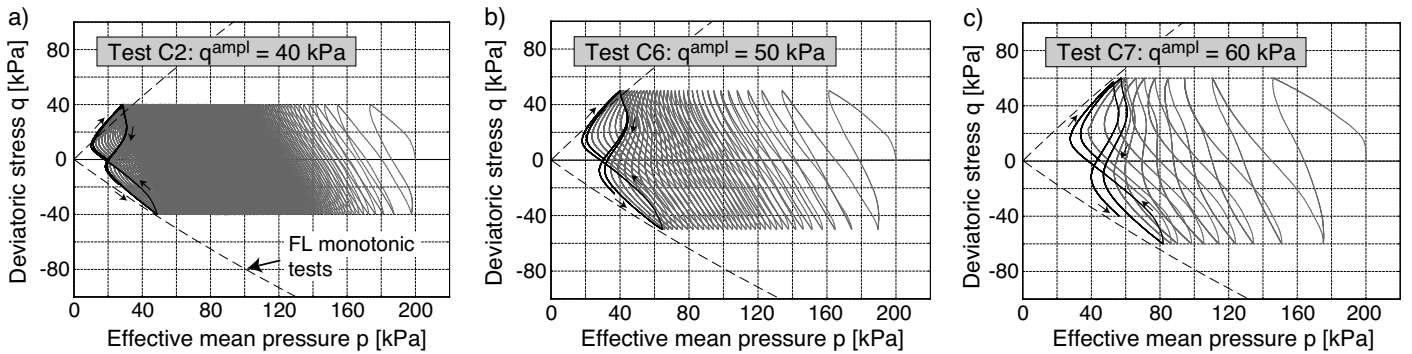

Fig. 7: Effective stress paths in the p-q-plane in undrained cyclic tests with different stress amplitudes applied to samples consolidated isotropically (all tests: $OCR = 1$, $p_0 = 200$ kPa, $\eta_0 = 0$, $\dot{s} = 0.1$ mm/min)

tereses.

The final effective stress loops measured in the tests with different stress amplitudes are summarized in Figure 8a. Obviously, the lower the amplitude, the smaller is the distance of this final stress loop to the origin of the p-q plane. Figure 8a demonstrates that during the final phase of the test, the effective stress path approximately adapts to the failure lines derived from the undrained monotonic tests.

The curves of accumulated pore water pressure $u^{\mathrm{acc}}(N) = u(N) - u(N = 0)$ normalized by the initial effective mean pressure p_0 are provided in Figure 9a. In order to evaluate $u^{\mathrm{acc}}(N)$, back pressure $u(N = 0)$ is subtracted from the pore water pressure $u(N)$ measured at the end of cycle No. N. A ratio $u^{\mathrm{acc}}/p_0 = 1$ corresponding to zero effective stress has not been reached in the present tests on Kaolin (Figure 9a). As expected, the accumulation of pore water pressure and thus the relaxation of mean effective stress runs faster with increasing stress amplitude, which is in good agreement with the literature [5–8, 12–14, 16, 17, 23, 24, 30, 42, 43, 46, 49–54, 66–69, 75, 76, 84, 86, 88, 92, 103, 105, 124, 133, 136, 137].

Figure 9b presents the amplitude-pressure-ratio $q^{\mathrm{ampl}}/(2p_0)$ as a function of the number of cycles N_f to failure, corresponding to an axial strain $|\varepsilon_1| = 10\%$. The horizontal arrow at the data point for $q^{\mathrm{ampl}} = 30$ kPa indicates that this sample did not fail within the 4368 applied cycles. This test has been stopped due to time limitations. The initial void ratios e_0 given near the symbols in Figure 9b range from 1.121 to 1.252. Although a standardized sample preparation method has been used for all tests (Section 2), a certain scatter of the initial void

ratios e_0 could not be prevented. These variations in e_0 also cause the slightly different results obtained for tests with identical stress amplitude (Figure 9a,b).

Larger initial void ratios lead to larger strain amplitudes. Therefore, in Figure 9c instead of the stress amplitude q^{ampl} the axial strain amplitude $\varepsilon_1^{\mathrm{ampl}}(N = 2)$ measured in the second cycle is used on the ordinate (note that $\varepsilon_1^{\mathrm{ampl}}$ continuously increases throughout a test, Figure 6b). An almost unique relationship between $\varepsilon_1^{\mathrm{ampl}}(N = 2)$ and N_f can be concluded from Figure 9c. Looking at the data for the pairs of tests performed with the same amplitude ($q^{\mathrm{ampl}} = 45$ kPa or 50 kPa), the tests with the larger strain amplitude showed failure in a lower number of cycles. Therefore, the differences in the cumulative rates are primarily caused by the different strain amplitudes, which in turn arise from the scatter of initial void ratios. In most tests of the present study, larger initial void ratios lead to a lower secant stiffness and thus larger strain amplitudes. The pair of tests with $q^{\mathrm{ampl}} = 45$ kPa is the only exception to this rule, probably due to the natural scatter of experimental data.

The secant Young's modulus $E = q^{\mathrm{ampl}}/\varepsilon_1^{\mathrm{ampl}}$ at $N = 2$ or $N = 5$, respectively, derived from the tests with different amplitudes is further inspected in Figure 9d, where it has been divided by a void ratio function $f_{E,e}$ and plotted versus the corresponding strain amplitude $\varepsilon_1^{\mathrm{ampl}}$. The void ratio function $f_{E,e} = (a - e)^2/(1 + e)$ with $a = 4.4$ has been derived from the data given in Figure 11h, that means from the test series with a variation of frequency (Section 4.2). Data from tests C32-C36 with a variation of stress amplitude at anisotropic stresses ($\eta_0 = 0.375$), discussed further
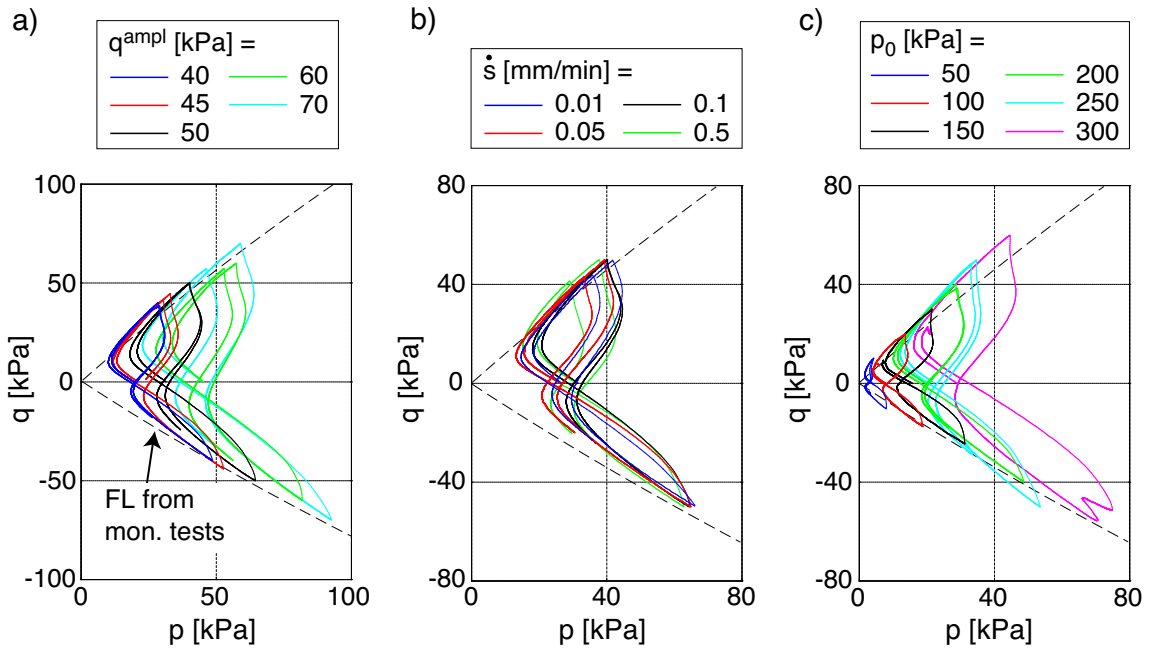
Fig. 8: *Summary of final effective stress loops in tests with different a) stress amplitudes q^{ampl}, b) displacement rates $\dot{s}$ and c) initial effective mean pressures p_0*
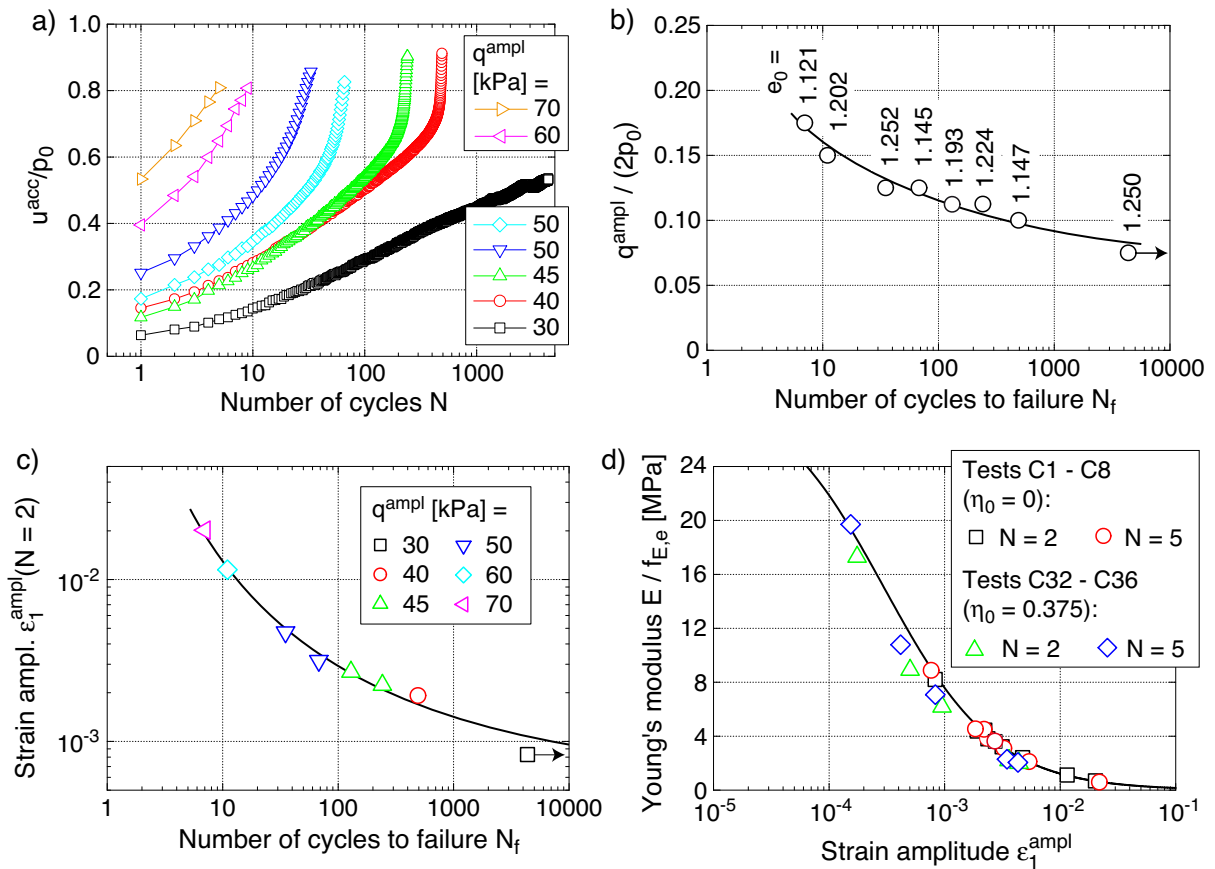

Fig. 9: *Results from tests with different stress amplitudes at isotropic consolidation stresses (all tests: $OCR = 1$, $p_0 = 200$ kPa, $\eta_0 = 0$, $\dot{s} = 0.1$ mm/min): a) Normalized accumulated pore water pressure u^{acc}/p_0 as a function of the number of cycles, b) Amplitude-pressure ratio $q^{ampl}/(2p_0)$ versus number of cycles to failure N_f, c) Strain amplitude $\varepsilon_1^{ampl}(N = 2)$ versus N_f, d) Secant Young's modulus $E/f_{E,e}$ in dependence of strain amplitude ε_1^{ampl} with void ratio function $f_{E,e} = (a - e)^2/(1 + e)$ with $a = 4.4$*

in Section 4.5, are also included in Figure 9d. The strong decrease of E with increasing strain amplitude $\varepsilon_1^{\mathrm{ampl}}$ can be e.g. described by an equation similar to that proposed by Stokoe et al. [112]:

$$\frac{E}{E_{\mathrm{max}}} \;=\; f_{E,\mathrm{ampl}} \;=\; \frac{1}{1 + (\varepsilon_1^{\mathrm{ampl}}/\varepsilon_{1,r}^{\mathrm{ampl}})^\alpha} \qquad (1)$$

with a reference strain amplitude $\varepsilon_{1,r}^{\mathrm{ampl}} = 3 \cdot 10^{-4}$ (corresponding to $f_{E,\mathrm{ampl}} = 0.5$) and an exponent $\alpha = 0.90$ (solid curve in Figure 9d). Note that the small strain stiffness E_{max} of the Kaolin has not been measured in the present study. From an extrapolation of the data in Figure 9d (i.e. a curve-fitting of Eq. (1) to the data) a value $E_{\mathrm{max}}/f_{E,e} \approx 30$ MPa is derived. Experimental studies on the stiffness of clay at small to moderate strains are documented e.g. in [21, 22, 27, 31, 33, 41, 55, 57–60, 63, 65, 70, 74, 79, 89, 93, 101, 104, 106, 108, 115, 119–121, 135]. Likewise, a threshold strain amplitude below which no cumulative effects occur [24, 49, 50, 124] has not been examined in the present study.

4.2 Variation of displacement rate

Two test series with a variation of the displacement rate (i.e. the loading frequency) have been performed, the first one using a stress amplitude of $q^{\mathrm{ampl}} = 45$ kPa (six tests with displacement rates $\dot{s}$ between 0.01 and 0.5 mm/min, tests C3-C4 and C9-C12 in Table 2) and the second one with $q^{\mathrm{ampl}} = 50$ kPa (five tests with $0.01 \leq \dot{s} \leq 0.5$ mm/min, tests C5-C6 and C13-C15 in Table 2). All samples were isotropically consolidated at $p_0 = 200$ kPa.

The effective stress paths for three different displacement rates (0.01, 0.05 and 0.5 mm/min) at $q^{\mathrm{ampl}} = 50$ kPa presented in Figure 10 look almost identical. Similar conclusions can be drawn also from Figure 8b where the final effective stress loops measured in the test series with $q^{\mathrm{ampl}} = 50$ kPa are compiled. The same applies to the stress-strain hystereses not shown herein.

The pore pressure accumulation curves $u^{\mathrm{acc}}(N)$ in Figures 11a,b do not show any clear correlation with the displacement rate. The diagrams in Figure 11c,d show the number of cycles to failure versus the displacement rate $\dot{s}$. The scatter of data in these diagrams is again primarily caused by variations in the initial void ratios. With the exception of the tests C3 and C4 at 0.1 mm/min in Figure 11c, that were already addressed in the last section, the data points lying at the lower bound of the data in Figure 11c,d correspond to higher void ratios and thus larger strain amplitudes.

In order to separate the effects of displacement rate and void ratio / strain amplitude, the presentation of the data in Figure 11e,f is useful. In those diagrams the strain amplitude in the second cycle (the amplitude in another cycle could have been used as well) is plotted versus the number of cycles to failure. The solid curves in Figure 11e,f have been constructed based on the data of the two tests with 0.1 mm/min available in each test series and the shape of the curves $\varepsilon_1^{\mathrm{ampl}}(N_f)$ known from Figure 9c. Considering a constant strain amplitude in Figure 11e,f it can be concluded that the differences between the data for the higher loading rates $\dot{s} = 0.05$, 0.1 and 0.5 mm/min are rather small. For the lower rates $\dot{s} = 0.01$ and 0.02 mm/min, however, the diagrams in Figure 11e,f give hints that the N_f values get lower

with decreasing displacement rate. This means a slight increase in the cumulative rates with decreasing $\dot{s}$. The low frequency dependence of the cumulative effects compared to other studies in the literature is probably due to the relatively low plasticity of the tested Kaolin. It coincides well with the results from the monotonic tests (Figure 4c,d). In agreement with the tendency in Figure 11e,f, most of the experimental investigations on cohesive soils in the literature found an acceleration of the accumulation of pore water pressure or residual strain when the loading frequency was reduced [5, 6, 10, 15, 42, 46, 69, 84, 95, 114, 122, 136, 137]. Only a limited number of studies came to the opposite conclusion [134] or did not find any rate effects [51, 64].

The Young's modulus obtained from the tests with a variation of the displacement rate is analysed in Figure 11g,h. The stiffness has been divided by the amplitude function $f_{E,\mathrm{ampl}}$ defined by Eq. (1) in order to purify the data from the influence of strain amplitude. A decrease of E with increasing initial void ratio e_0 is obvious in Figure 11g,h. The influence of the displacement rate $\dot{s}$ on E is rather small. The data in Figure 11h have been used to derive the function $f_{E,e} = (a - e)^2/(1 + e)$ with a parameter $a = 4.4$. It is applied for a normalization of the stiffness in several diagrams in this paper.

4.3 Variation of initial mean pressure p_0

The influence of the initial effective mean pressure p_0 was studied in eight tests with isotropic consolidation at 50 kPa $\leq p_0 \leq 300$ kPa (tests C2 and C16-C22 in Table 2). All samples were subjected to a cyclic loading with an amplitude-pressure ratio $\zeta = q^{\mathrm{ampl}}/p_0 = 0.2$ and a displacement rate $\dot{s} = 0.1$ mm/min. The effective stress paths measured in the three tests with $p_0 = 50$, 100 and 300 kPa are shown in Figure 12. These paths show similar characteristics as that obtained in the test C2 with $p_0 = 200$ kPa given in Figure 7a.

The final effective stress loops observed in the tests with different p_0 values are collected in Figure 8c. Similar as in the test series with a variation of the amplitude, these stress paths approximately adapt to the failure lines derived from the undrained monotonic tests. Consequently, the lower amplitudes chosen in the tests with smaller initial pressures lead to a smaller distance of the final effective stress loop to the origin of the p-q plane.

The curves $u^{\mathrm{acc}}(N)/p_0$ of this test series are collected in Figure 13a. In Figure 13b the number of cycles to failure is plotted versus p_0. A possible dependence of N_f on p_0 is masked by the variations in the initial void ratios. The pressure dependence of the cumulative rates can be better judged based on Figure 13c where the strain amplitudes $\varepsilon_1^{\mathrm{ampl}}(N = 2)$ have been plotted versus N_f. The pressure dependence of stiffness and the fluctuating initial void ratios lead to a relatively large range of measured strain amplitudes $10^{-3} \leq \varepsilon_1^{\mathrm{ampl}}(N = 2) \leq 2.2 \cdot 10^{-3}$. The curves $\varepsilon_1^{\mathrm{ampl}}(N_f)$ added for the different pressures in Figure 13c are based upon the curve in Figure 9c. Considering a constant value of the strain amplitude $\varepsilon_1^{\mathrm{ampl}}(N = 2)$, the increase in the number of cycles to failure with increasing value of p_0 is evident in Figure 13c.

Finally, the pressure dependence of the secant stiffness is inspected in Figure 13d. The values of Young's modulus derived from the data of the cycles Nos. 2 and 5 have been divided by the void ratio function $f_{E,e}$ and the amplitude
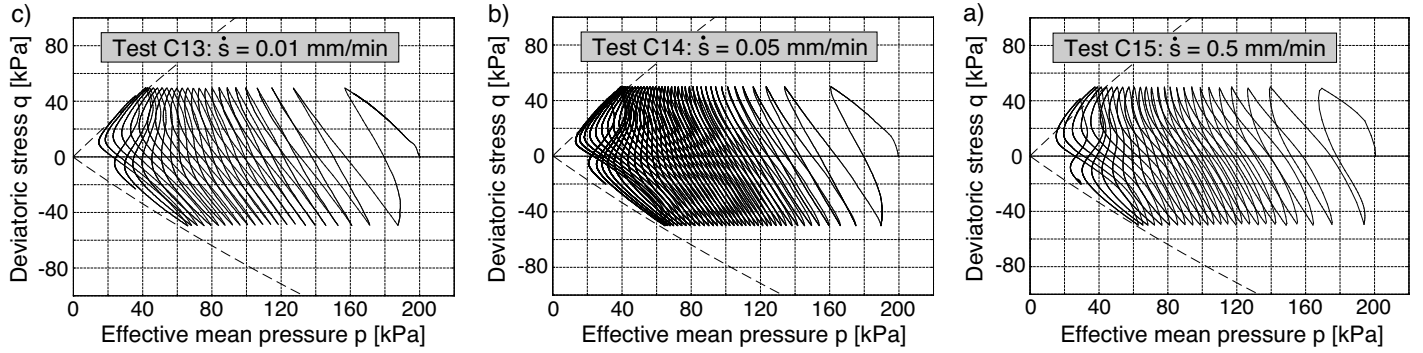
Fig. 10: Effective stress paths in the p-q-plane measured in the tests with different displacement rates $\dot{s}$ (all tests: $OCR = 1$, $p_0 = 200$ kPa, $\eta_0 = 0$, $q^{\text{ampl}} = 50$ kPa)

function $f_{E,\text{ampl}}$ in order to obtain the pure influence of pressure. Based on the data in Figure 13d, this influence can be described by $E \sim (p_0/p_{\text{atm}})^{0.8} p_{\text{atm}}$ with atmospheric pressure $p_{\text{atm}} = 100$ kPa.

4.4 Variation of initial stress ratio η_0

Ten samples were all consolidated at $p_0 = 200$ kPa but with different initial stress ratios $\eta_0 = q_0/p_0$ between -0.5 and 0.625. The stress amplitude was $q^{\text{ampl}} = 30$ kPa and the displacement rate was $\dot{s} = 0.1$ mm/min in all tests. The testing programme is given as tests C1 and C23-C27 (triaxial compression, i.e. $\eta_0 \geq 0$) and C28-C31 (triaxial extension, $\eta_0 < 0$) in Table 2.

A typical result from a test with anisotropic consolidation in the triaxial compression regime ($\eta_0 = 0.375$, test C25) is shown in Figure 14. In that test the minimum deviatoric stress $q^{\text{min}} = q^{\text{av}} - q^{\text{ampl}}$ was positive, i.e. the effective stress path (Figure 14d) did not cross the p-axis. After a certain number of cycles the accumulated pore pressure almost stabilized at $u \ll \sigma_3$ (Figure 14a). A considerable accumulation of permanent axial strain was observed while the axial strain amplitude remained almost constant (Figure 14b,c). The accumulation of strain continued even after the pore pressure accumulation had stopped. In contrast to the tests with isotropic consolidation, the failure criterion $|\varepsilon_1| = 10$ % was reached due to excessive *permanent* axial strains, and not due to too large strain amplitudes. Such dependence of the failure mode on initial stress ratio is in accordance with the literature [5–8,52,67,76]. The effective stress path repeatedly passed through after the pore water pressure had become stable is lens-shaped (Figure 14d) with the maximum near the failure line from the monotonic tests (similar as observed in [53,76,103]).

Some of the effective stress paths measured in the other tests within this series are collected in Figure 15. The stress loop during the final stage of the test is again highlighted in black colour, while the rest of the path is formatted in grey. The p-q data for $\eta_0 = 0.625$ (not shown herein) look similar to those for $\eta_0 = 0.5$ (Figure 15a) and those for $\eta_0 = -0.125$ do not differ much from the effective stress paths provided for $\eta_0 = 0.125$ and $\eta_0 = -0.25$ (Figure 15c,d). Note that in all tests with $-0.25 \leq \eta_0 \leq 0.125$ the cyclic loading was stopped at relatively large numbers of cycles, before a stabilization of the accumulated pore water pressure or failure had been reached. In those tests further cycles would have led to a further relaxation of effective mean stress, i.e. the final position of the effective stress loop has not

been reached. The effective stress loops measured during the last cycles in the test with $\eta_0 = 0.125$ (Figure 15c) have the form of a narrow eight. This indicates that in the tests with shear stress reversals some kind of eight-shaped loops would have been probably obtained also near failure, similar to the case $\eta_0 = 0$ (Figure 7). Figure 15 reveals that in the tests with anisotropic consolidation, but without shear stress reversal, the effective stress paths repeatedly passed through after the accumulated pore water pressure had become stable are lens-shaped. The orientation with which these lenses are passed through is, however, opposite in triaxial compression (clockwise) and extension (counterclockwise). Interestingly, the strong inclination of the effective stress path observed in the triaxial compression tests is maintained also in the extension regime. This is in contrast to undrained cyclic triaxial tests on sand where the inclination of the stress path was observed opposite in triaxial extension and compression [130,131]. This strong inclination of the stress path is a sign of a pronounced inherent anisotropy of the tested material which is further discussed in Section 4.7.

Figure 16 summarizes the final effective stress loops measured in the tests of this series. If the samples came to failure the maximum (triaxial compression) or minimum (triaxial extension) deviatoric stresses within the lenses lay near to the failure lines observed in the monotonic tests.

The normalized pore pressure accumulation curves $u^{\text{acc}}(N)/p_0$ from the tests with triaxial compression (Figure 17a) show a moderate increase in the rate of pore pressure accumulation with increasing initial stress ratio. Simultaneously, the rate of deviatoric strain accumulation grows considerably with η_0 (Figure 17b). The cyclic tests with consolidation in the triaxial extension regime show a somewhat different tendency: While the deviatoric strain accumulation ($\dot{\varepsilon}_q^{\text{acc}} < 0$) becomes faster with increasing absolute value of the initial stress ratio $|\eta_0|$ (Figure 17c), the rate of pore water pressure accumulation decreases with $|\eta_0|$ (not shown in Figure 17). These observations are a result of the so-called "cyclic flow rule" or "direction of accumulation", which is discussed in more detail later in this section.

The dependence of the number of cycles to failure on the initial stress ratio η_0 is inspected in Figure 17d,e. Figure 17d presents the N_f values versus η_0. The vertical arrows denote that these tests have been stopped at larger N values before failure had been reached. A decrease of the number of cycles to failure with increasing absolute value of the initial stress ratio is obvious in Figure 17d. It is in good
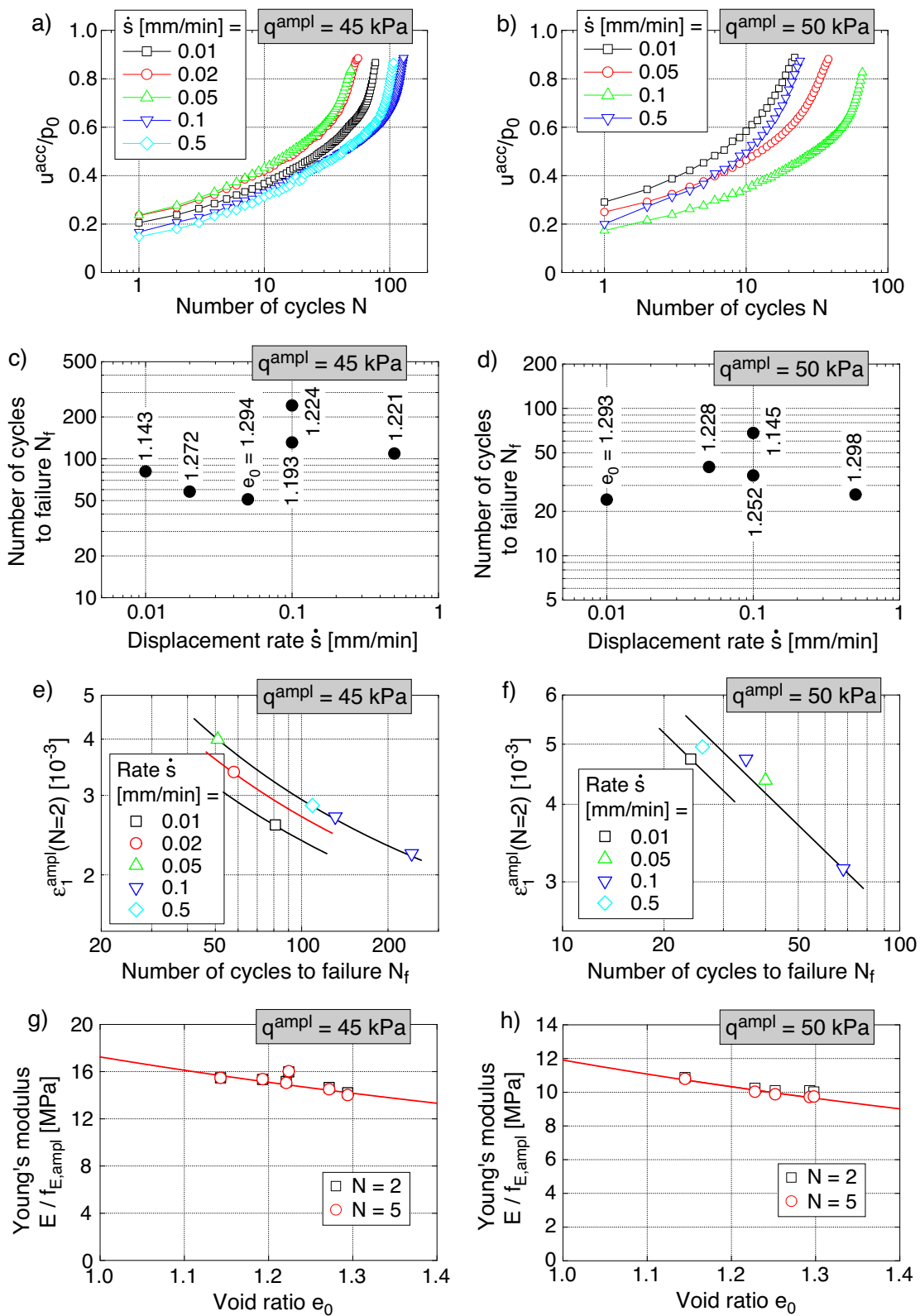
Fig. 11: *Results from tests with different displacement rates $\dot{s}$ and stress amplitudes q^{ampl} = 45 kPa (left-hand side) or q^{ampl} = 50 kPa (right-hand side): a,b) Normalized pore pressure accumulation curves $u^{acc}(N)/p_0$, c,d) Number of cycles to failure N_f versus displacement rate $\dot{s}$, e,f) Strain amplitude $\varepsilon_1^{ampl}(N = 2)$ versus N_f, g,h) Secant Young's modulus $E/f_{E,ampl}$ in dependence of displacement rate $\dot{s}$ (all tests: OCR = 1, p_0 = 200 kPa, η_0 = 0)*
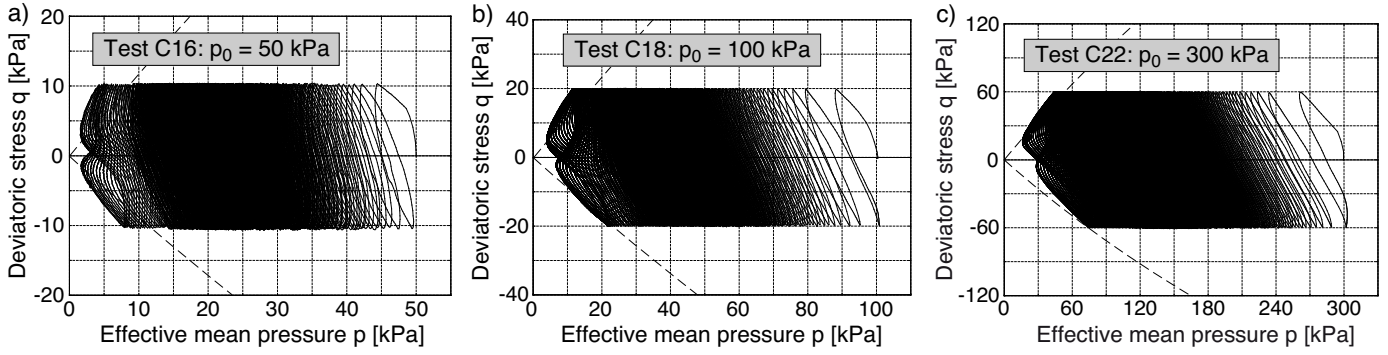
Fig. 12: Effective stress paths in the p-q-plane measured in tests with different initial mean pressures p_0 (all tests: $\eta_0 = 0$, $\zeta = q^{\mathrm{ampl}}/p_0$ = 0.2, $\dot{s}$ = 0.1 mm/min)
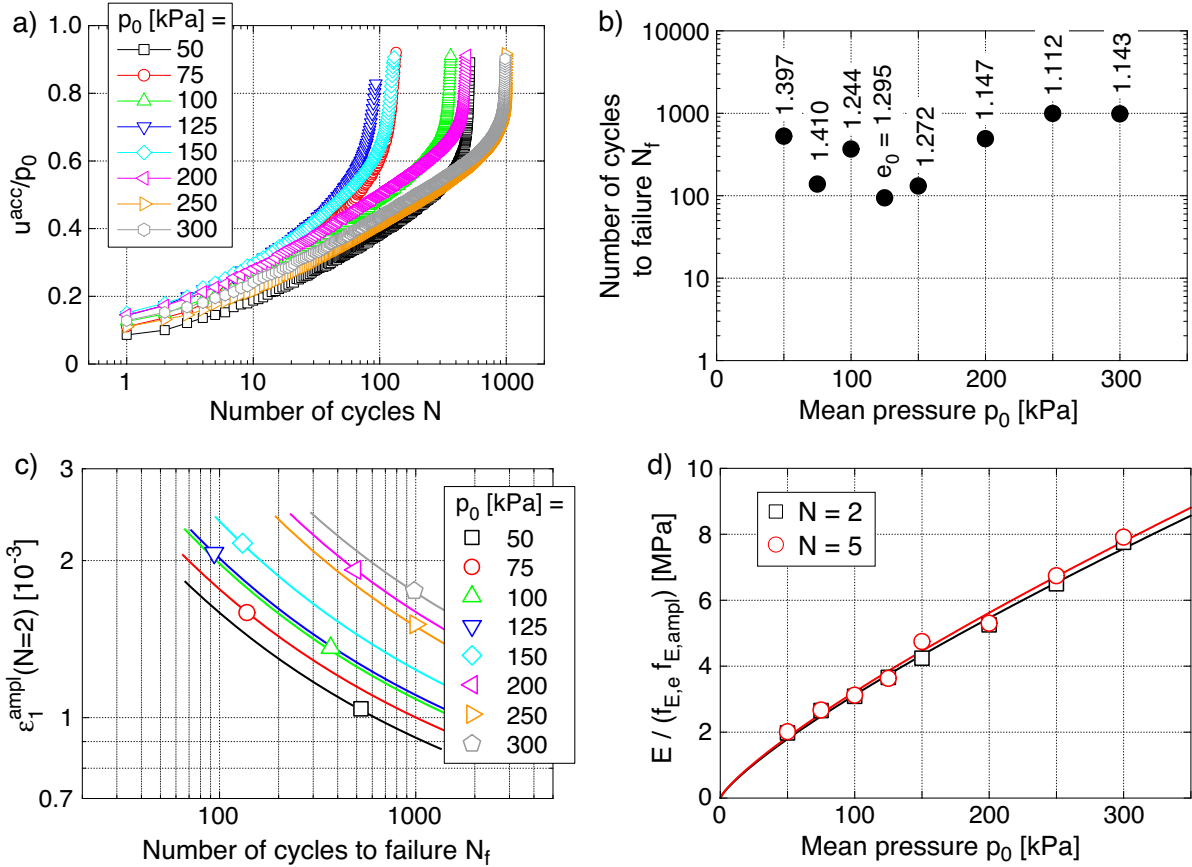
Fig. 13: Results from tests with different initial mean pressures p_0: a) Normalized pore pressure accumulation curves $u^{\mathrm{acc}}(N)/p_0$, b) number of cycles to failure N_f versus p_0, c) strain amplitude $\varepsilon_1^{\mathrm{ampl}}(N = 2)$ versus N_f, d) secant Young's modulus $E/(f_{E,e}f_{E,\mathrm{ampl}})$ in dependence of p_0 (all tests: $\eta_0 = 0$, $\zeta = q^{\mathrm{ampl}}/p_0 = 0.2$, $\dot{s} = 0.1$ mm/min)

accordance with [4,7,8,10,14,34,52,53,67,92,105,105,138]. Figure 17f demonstrates that this decrease is partly due to the increase in the strain amplitude with $|\eta_0|$, caused by the decrease of Young's modulus. Consequently, in Figure 17e the N_f data are analysed with respect to the strain amplitude $\varepsilon_1^{\mathrm{ampl}}(N = 2)$. Although the available data in Figure 17e are limited, a lower number of cycles to failure for higher $|\eta_0|$ values can be concluded for $\varepsilon_1^{\mathrm{ampl}}(N = 2)$ = constant.

In the following, the so-called "cyclic flow rule", i.e. the ratio between the volumetric and deviatoric components of the strain or stress accumulation rates is analysed. For con-

venience, the following discussion is undertaken in terms of strain rates. While the rate of deviatoric strain accumulation $\dot{\varepsilon}_q^{\mathrm{acc}} \approx \Delta\varepsilon_q^{\mathrm{acc}}/\Delta N$ can be directly derived from the test data, the measured rate of pore pressure accumulation $\dot{u}^{\mathrm{acc}} \approx \Delta u^{\mathrm{acc}}/\Delta N$ has to be converted to a rate of volumetric strain accumulation, using the relationship $\dot{\varepsilon}_v^{\mathrm{acc}} = \dot{u}^{\mathrm{acc}}/K$ with bulk modulus K. Since drained cyclic test data were not available for the Kaolin (compare [127]), the bulk modulus has been determined from the unloading curve measured in a stress-controlled oedometric compression test and described by:

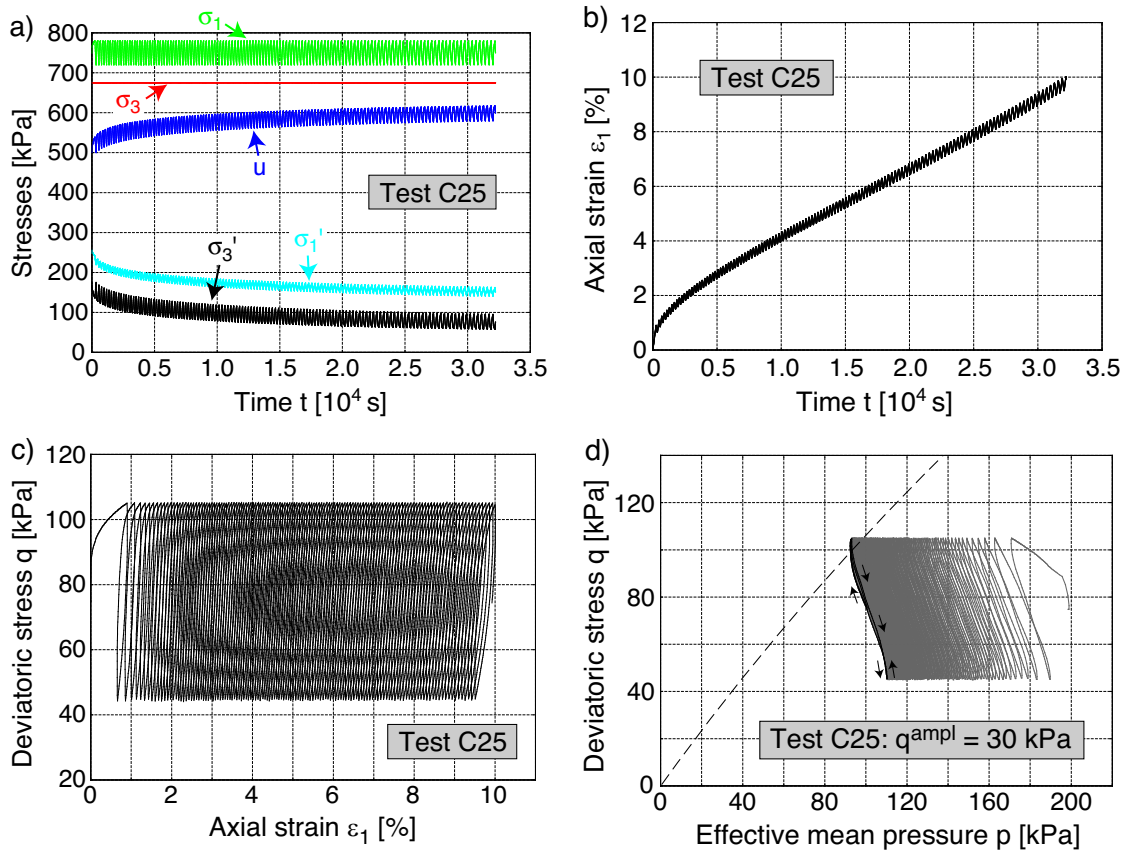$$K = 35 \ (p/p_{\mathrm{atm}})^{1.0} \ p_{\mathrm{atm}} = 35 \ p \qquad (2)$$

Fig. 14: Typical results of an undrained cyclic test with anisotropic consolidation (test C25 in Table 2 with $OCR = 1$, $p_0 = 200$ kPa, $\eta_0 = 0.375$, $q^{\mathrm{ampl}} = 30$ kPa, $\dot{s} = 0.1$ mm/min): a) Total or effective stress components and pore water pressure as a function of time t, b) axial strain ε_1 as a function of time t, c) deviatoric stress q versus axial strain ε_1, d) effective stress path in the p-q plane
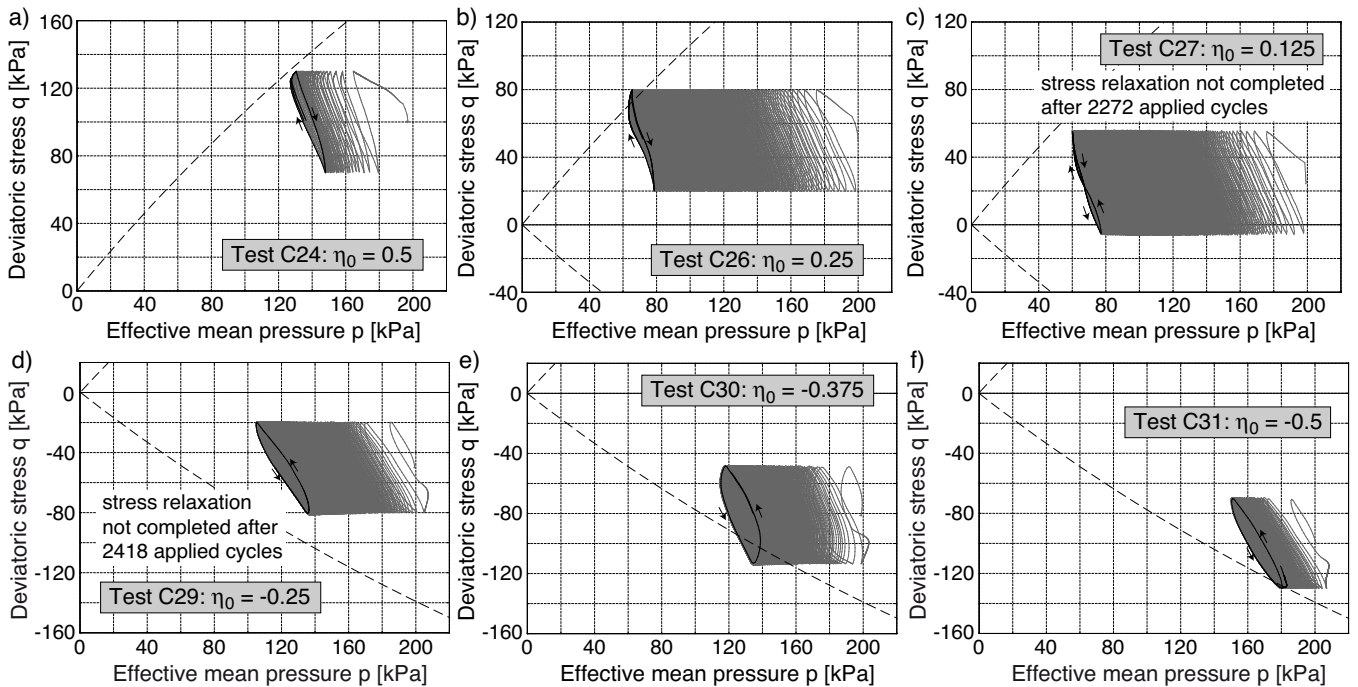

Fig. 15: Effective stress paths in the p-q-plane measured in tests with different initial stress ratios η_0 (all tests: $OCR = 1$, $p_0 = 200$ kPa, $q^{\mathrm{ampl}} = 30$ kPa, $\dot{s} = 0.1$ mm/min)
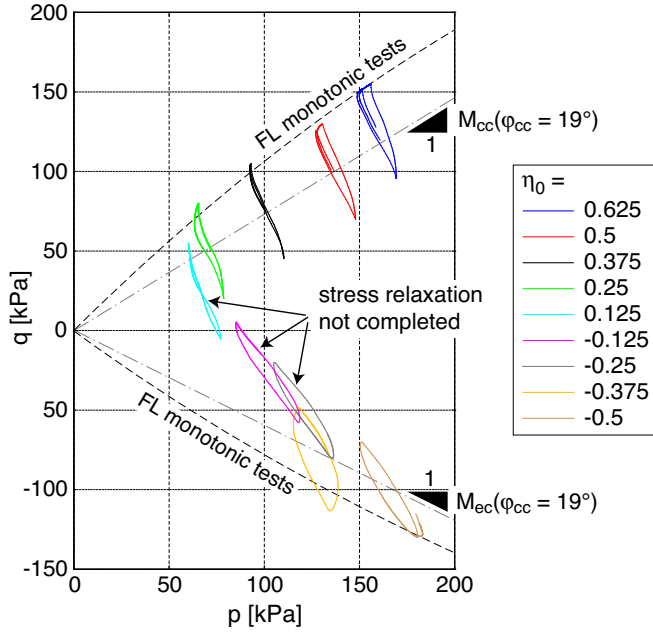
Fig. 16: *Summary of final effective stress loops in tests with different initial stress ratios η_0*

Eq. (2) has been used to convert $\dot{u}^{\rm acc}$ to $\dot{\varepsilon}_v^{\rm acc}$.

With the rates $\dot{\varepsilon}_q^{\rm acc}$ and $\dot{\varepsilon}_v^{\rm acc}$ evaluated for all tests within the series with a variation of η_0, the direction of accumulation can be illustrated by means of vectors in the p-q-plane (Figure 18). They are inclined by $1/\omega = \dot{\varepsilon}_q^{\rm acc}/\dot{\varepsilon}_v^{\rm acc}$ towards the horizontal. Due to the relaxation of mean effective stress at $q^{\rm av} = $ constant, the origin of these vectors is shifted to the left with increasing number of cycles. Figure 18 demonstrates that similar to sand [128], the deviatoric portion of strain accumulation becomes larger with increasing absolute value of the average stress ratio $\eta^{\rm av}$, that means the vectors show a larger inclination for higher $|\eta^{\rm av}|$-values. The negative inclination of the vectors on the isotropic axis ($\eta = 0$, data for vertical cutting direction) indicates that the cyclic flow rule of Kaolin is anisotropic. This manifests itself in the negative deviatoric strain accumulation rates measured in the tests with isotropic consolidation (see $\varepsilon_q^{\rm acc}(N)$ curve for $\eta_0 = 0$ in Figure 17b). Note that the accumulated strain is defined as the strain remaining after the completion of a full cycle. The stress-strain relationship in Figure 6c reveals that although the axial strain $\varepsilon_1^{\rm max}$ at the maximum deviatoric stress $q^{\rm max}$ during a cycle is significantly larger than the absolute value of $\varepsilon_1^{\rm min}$ at $q^{\rm min}$ (i.e. $(\varepsilon_1^{\rm max} + \varepsilon_1^{\rm min})/2 > 0$), the axial strain $\varepsilon_1^{\rm acc}$ after the completion of a full cycle (i.e. at $q = 0$ coming from the extension side, $q < 0$) is negative. Since in an undrained test $\varepsilon_q = \varepsilon_1$ applies due to $\varepsilon_v = 0$, a negative value of $\varepsilon_1^{\rm acc}$ implies $\varepsilon_q^{\rm acc} < 0$.

Another illustration of the cyclic flow rule is provided in Figure 19. In those diagrams the strain rate ratio $\omega = \dot{\varepsilon}_v^{\rm acc}/\dot{\varepsilon}_q^{\rm acc}$ (Figure 19a) or its reciprocal value (Figure 19b) are plotted versus the actual stress ratio $\eta^{\rm av}$. Figure 19 corroborates the increase in the deviatoric portion of the rate of strain accumulation with increasing $|\eta^{\rm av}|$. An isotropic accumulation ($\dot{\varepsilon}_v^{\rm acc} \neq 0$ or $\dot{u}^{\rm acc} \neq 0$ and $\dot{\varepsilon}_q^{\rm acc} = 0$) can be expected at a stress ratio $\eta_{\rm iso} \approx 0.10$. A purely deviatoric accumulation ($\dot{\varepsilon}_v^{\rm acc} = 0$ or $\dot{u}^{\rm acc} = 0$ and $\dot{\varepsilon}_q^{\rm acc} \neq 0$) is ob-

tained at $\eta^{\rm av} \approx 0.75$ in the triaxial compression regime and at $\eta^{\rm av} \approx -0.6$ for triaxial extension.

As demonstrated by the black solid curves in Figure 19, the measured strain rate ratios $\omega = \dot{\varepsilon}_v^{\rm acc}/\dot{\varepsilon}_q^{\rm acc}$ are well approximated by the generalized anisotropic flow rule proposed in [129] using the parameters $\eta_{\rm iso} = 0.10$, $\varphi_{cc} = 19°$ and $n_g = 0.1$. The equations of this generalized flow rule are provided in the Appendix. Such flow rule is capable to predict cumulative extensional strains at $\eta^{\rm av} = 0$, i.e. it can reproduce the flow rule vectors on the p-axis being inclined towards the extension regime of the p-q plane (Figure 18, data for samples cut out vertically). The flow rule of the modified Cam clay (MCC) model

$$\frac{\dot{\varepsilon}_v^{\rm acc}}{\dot{\varepsilon}_q^{\rm acc}} \;\; = \;\; \frac{M^2 - (\eta^{\rm av})^2}{2\eta^{\rm av}} \tag{3}$$

with $M = \dfrac{6\sin\varphi_{cc}}{3 - \sin\varphi_{cc}}$ and $\varphi_{cc} = 19°$ is slightly less accurate regarding the reproduction of the measured $\dot{\varepsilon}_v^{\rm acc}/\dot{\varepsilon}_q^{\rm acc}$ data (see dashed black curves in Figure 19). Furthermore, it predicts a purely volumetric accumulation for isotropic average stresses.

4.5 Variation of stress amplitude at anisotropic consolidation stresses

Analogously to the test series described in Section 4.1, the influence of the stress amplitude was also studied on samples consolidated anisotropically ($p_0 = 200$ kPa, $\eta_0 = 0.375$). All six samples (tests C25 and C32-C36 in Table 2) were subjected to a cyclic loading with a displacement rate $\dot{s} = 0.1$ mm/min. The stress amplitudes lay within the range 15 kPa $\leq q^{\rm ampl} \leq$ 40 kPa. Figure 20 presents the effective stress paths from the tests with $q^{\rm ampl} = 20$, 30 and 40 kPa. The area encompassed by the effective stress path in the p-q-plane during the last cycle increases with increasing stress amplitude. Furthermore, the orientation of the stress path in this final lens reverses with increasing amplitude (counterclockwise for low amplitudes, clockwise for large ones). The summary of the final effective stress loops in Figure 21a reveals tentatively that lower mean pressures can be reached by stress cycles with lower amplitudes. This is in accordance with the isotropic case (Figure 8a).

Of course, also in these tests with anisotropic consolidation the rates of pore water pressure and deviatoric strain accumulation became larger with increasing $q^{\rm ampl}$. Figure 22 compares the data from both test series with a variation of stress amplitude, performed with either isotropic or anisotropic consolidation. Figure 22a reveals that looking at a certain amplitude-pressure ratio $q^{\rm ampl}/(2p_0)$, the samples consolidated anisotropically fail within a considerably lower number of cycles. As already visible in Figure 17e,f, the secant stiffness is lower and thus the strain amplitudes $\varepsilon_1^{\rm ampl}$ are higher for the samples consolidated anisotropically (Figure 22b). The higher strain amplitudes contribute to the lower numbers of cycles to failure observed for the anisotropically consolidated samples. If the strain amplitude $\varepsilon_1^{\rm ampl}(N = 2)$ is plotted on the ordinate instead of $q^{\rm ampl}/(2p_0)$ (Figure 22c), the curves for isotropic and anisotropic consolidation lie closer to each other than in Figure 22a (due to the higher $\varepsilon_1^{\rm ampl}(N = 2)$ values of the anisotropically consolidated samples for $q^{\rm ampl}/(2p_0) = $ constant). However, considering a constant strain ampli-
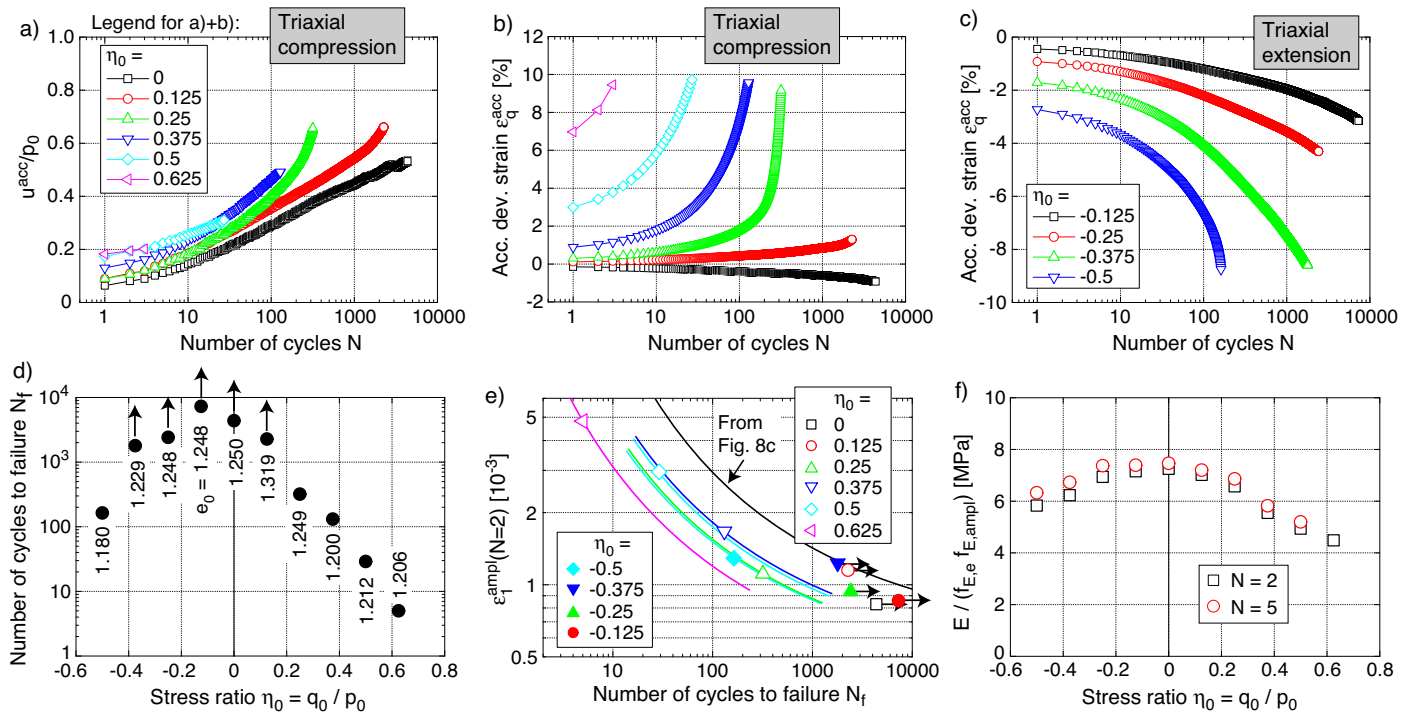
Fig. 17: *Results from tests with different initial stress ratios η_0: a) Normalized pore pressure accumulation curves $u^{acc}(N)/p_0$ in the tests with triaxial compression, b),c) Deviatoric strain accumulation curves $\varepsilon_q^{acc}(N)$ in the tests with triaxial compression or extension, d) Number of cycles to failure N_f versus η_0, e) Strain amplitude $\varepsilon_1^{ampl}(N = 2)$ versus N_f, f) Secant Young's modulus $E/(f_{E,e}f_{E,ampl})$ in dependence of η_0 (all tests: OCR = 1, p_0 = 200 kPa, q^{ampl} = 30 kPa, $\dot{s}$ = 0.1 mm/min)*
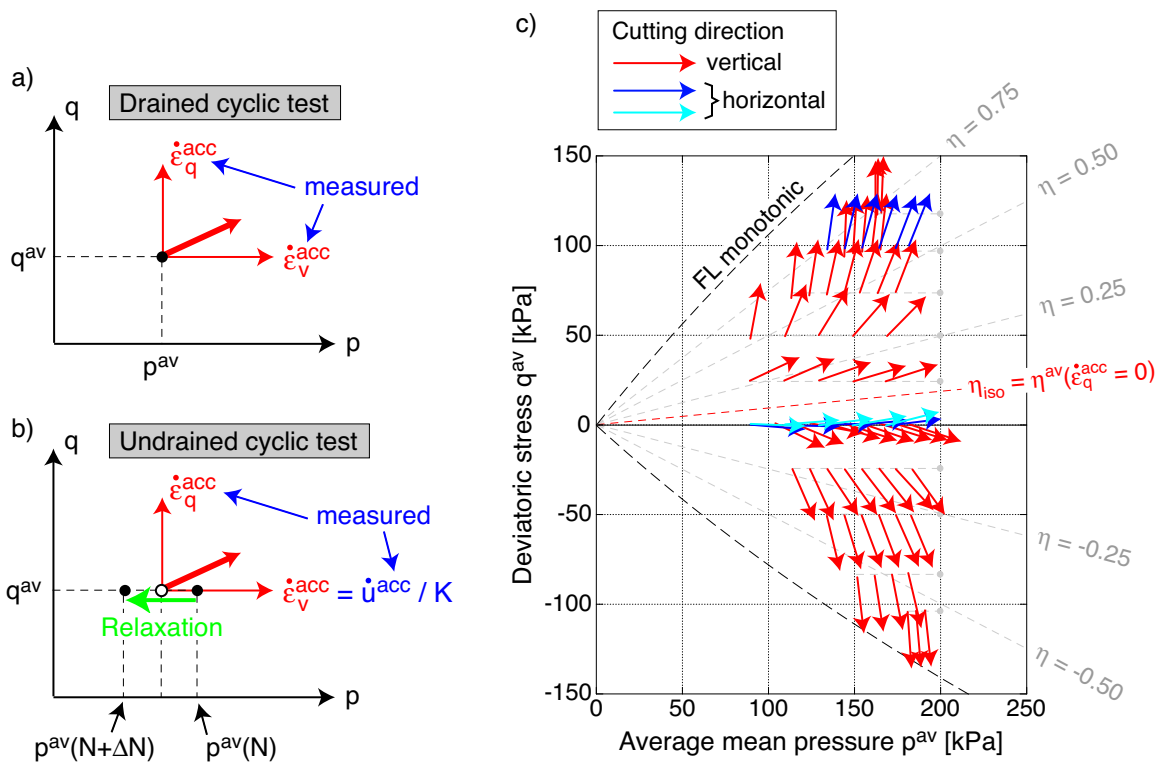
Fig. 18: *Direction of accumulation shown as vectors in the p-q-plane, derived from the tests with different initial stress ratios η_0*
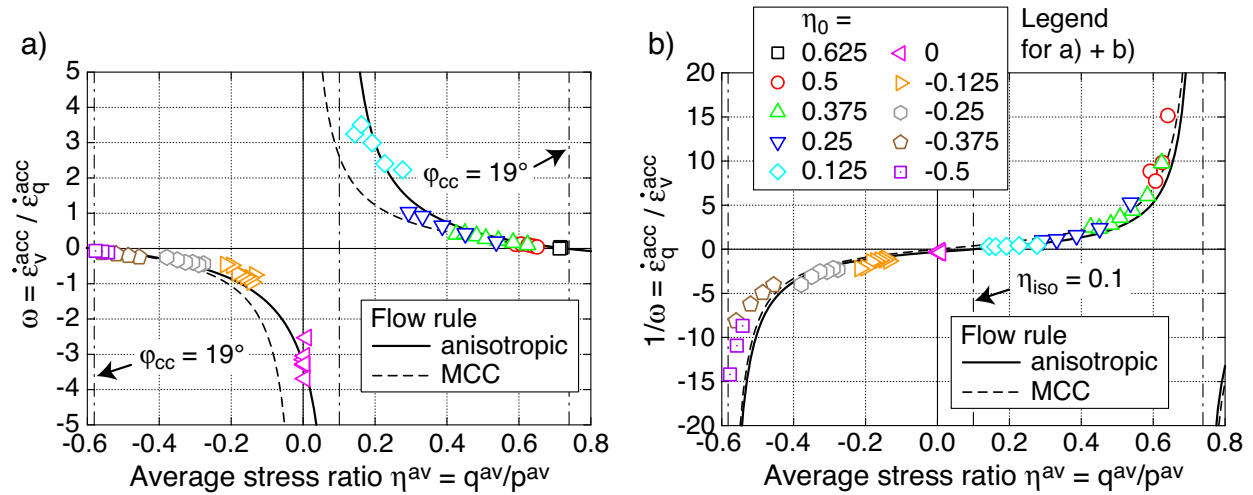
Fig. 19: a) Strain rate ratio $\omega = \dot{\varepsilon}_v^{acc}/\dot{\varepsilon}_q^{acc}$ and b) reciprocal value $1/\omega = \dot{\varepsilon}_q^{acc}/\dot{\varepsilon}_v^{acc}$ as a function of actual average stress ratio η^{av}. The data from the tests with different initial stress ratios η_0 is compared to the prediction by the MCC flow rule, Eq. (3), and the generalized anisotropic flow rule explained in Appendix.
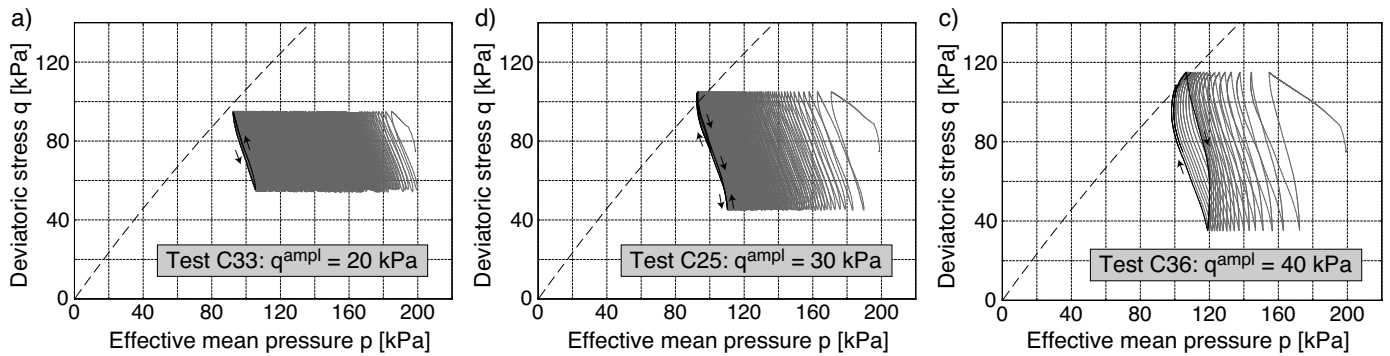

Fig. 20: Effective stress paths in the p-q-plane measured in undrained cyclic tests with different stress amplitudes q^{ampl} applied at anisotropic consolidation stresses (all tests: $OCR = 1$, $p_0 = 200$ kPa, $\eta_0 = 0.375$, $\dot{s} = 0.1$ mm/min)
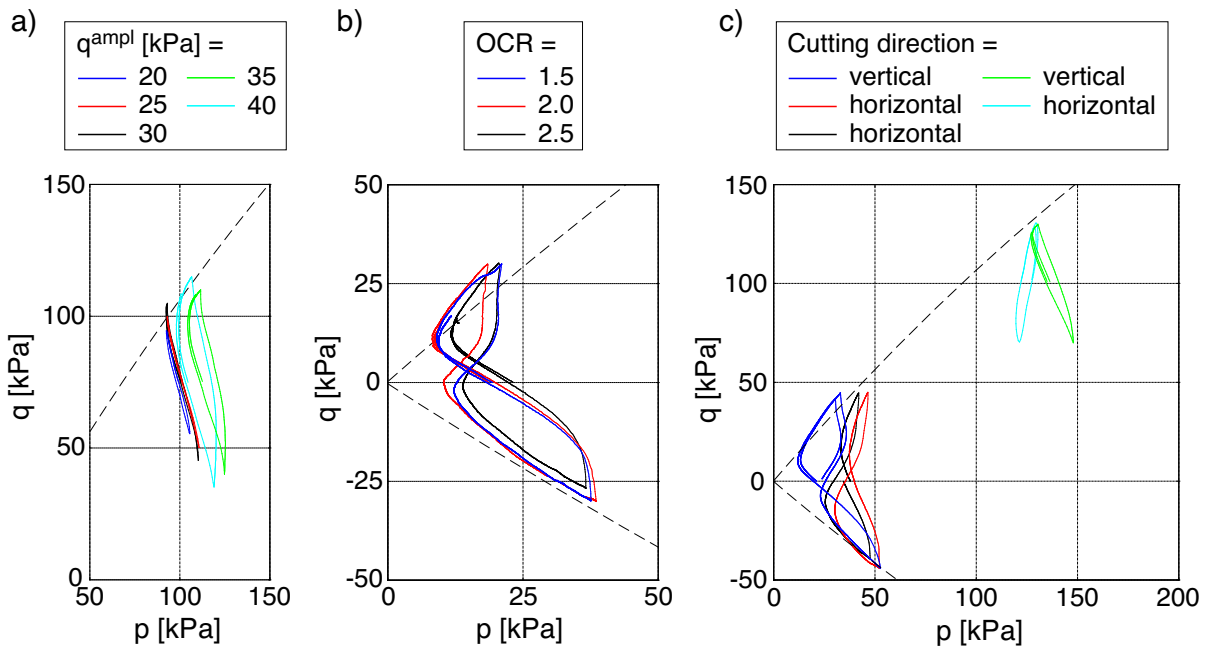

Fig. 21: Summary of final effective stress loops in tests with different a) stress amplitudes q^{ampl} at $\eta_0 = 0.375$, b) OCR values and c) cutting directions

tude $\varepsilon_1^{\mathrm{ampl}}(N = 2)$ in Figure 22c, the samples consolidated isotropically still withstand a larger number of cycles up to failure.

4.6 Variation of overconsolidation ratio OCR

Three tests were performed with overconsolidation ratios larger than 1 (tests C37-C39 in Table 2). The samples were isotropically consolidated in the triaxial cell to p_{max} = 150, 200 and 250 kPa followed by an unloading to p_0 = 100 kPa, resulting in OCR-values of 1.5, 2.0 and 2.5. The undrained cyclic loading with $q^{\mathrm{ampl}} = 30$ kPa and $\dot{s}$ = 0.1 mm/min started from p_0. The effective stress paths obtained from these three tests are provided in Figure 23. They look almost similar to those for $OCR = 1$. The only exception refers to the dilative response during the first cycle which was observed for the samples with $OCR > 1$. Consequently, the mean effective stress after the completion of the first cycle lay at $p > p_0$. The dilative tendency within the first cycle was found stronger for higher OCR values (cf. [9, 16, 77, 78, 81, 88, 123]). All subsequent cycles revealed a contractive response, however. No clear OCR dependence can be concluded from the summary of the final effective stress loops in Figure 21b.

In Figure 24a the curves $u^{\mathrm{acc}}(N)/p_0$ of pore water pressure accumulation start from negative values at $N = 1$ because of the dilative response in the first cycle mentioned above. The higher OCR the more negative is the initial value of $u^{\mathrm{acc}}(N)/p_0$. The positive rates $\dot{u}^{\mathrm{acc}} > 0$ at $N > 1$ confirm the contractive material response during all further cycles. Figure 24a further indicates, that the rate of pore pressure accumulation decreases with OCR. Consequently, the number of cycles to failure grows considerably with increasing OCR (Figure 24b). In order to eliminate the effect of different strain amplitudes, the $\varepsilon_1^{\mathrm{ampl}}(N = 2)$-$N_f$ diagram in Figure 24c has been prepared. The curve for $OCR = 1$ in Figure 24c has been overtaken from Figure 13c (curve for $p_0 = 100$ kPa). The curves $\varepsilon_1^{\mathrm{ampl}}(N_f)$ for the various OCR-values in Figure 24c should be seen as tentatively because they are based on a rather limited amount of data points. Nevertheless, examining a constant strain amplitude, considerably higher numbers of cycles to failure for the larger OCR-values can be also concluded from Figure 24c. This is in good agreement with [52, 77, 78, 88, 123]. The tests further demonstrated that the elastic stiffness is not significantly affected by the overconsolidation, at least in the range of tested OCR values (as may be also concluded from the almost constant strain amplitudes $\varepsilon_1^{\mathrm{ampl}}$ for identical stress amplitudes q^{ampl} shown in Figure 24c).

4.7 Samples cut out in the horizontal direction

In order to study effects of anisotropy, three samples were cut out from the pre-consolidated blocks in the horizontal direction while all other samples discussed so far were cut out vertically (Figure 25). In the triaxial cell two of these three samples were consolidated isotropically at p_0 = 200 kPa and $\eta_0 = 0$ (tests C40 and C41 in Table 2). The cyclic loading was applied with an amplitude q^{ampl} = 45 kPa and a displacement rate $\dot{s} = 0.1$ mm/min in both tests. The third sample (test C42 in Table 2) was consolidated anisotropically at $p_0 = 200$ kPa and $\eta_0 = 0.5$. The amplitude and the displacement rate were $q^{\mathrm{ampl}} = 30$ kPa and $\dot{s} = 0.1$ mm/min in that test. Figure 26 presents the

effective stress paths obtained in tests C41 and C42. Obviously, the inclination of the effective stress path is opposite to similar tests performed on samples cut out in the vertical direction (compare Figure 26a with Figure 7 and Figure 26b with Figure 15a). Also the final effective stress loop differs between both types of samples (Figure 21c). The orientation with which the final stress loop is passed through is, however, independent of the cutting direction (see the arrows in Figure 26).

Figure 27a presents the curves of accumulated pore water pressure $u^{\mathrm{acc}}(N)$ measured for the two isotropically consolidated samples. The data are compared to those of tests C3 and C4 with equal values of p_0, η_0 and q^{ampl}, but performed on vertical samples. The rates of pore pressure accumulation are much lower for the horizontal samples. Consequently, for a given amplitude-pressure ratio $q^{\mathrm{ampl}}/(2p_0)$, these samples can withstand a much larger number of cycles to failure than the vertical samples (Figure 27b). Figure 27c demonstrates, that the lower pore pressure accumulation rates measured for the horizontal samples are primarily a product of the lower strain amplitudes. For the same stress amplitude $q^{\mathrm{ampl}} = 45$ kPa, the strain amplitudes $\varepsilon_1^{\mathrm{ampl}}(N = 2)$ in tests C40 and C41 amount only about 60 % of the values observed in tests C3 and C4. Therefore, the sample response is stiffer if the cycles are applied perpendicular to the sedimentation and consolidation direction. The secant stiffness of the Kaolin thus shows a strong anisotropy. If the strain amplitude $\varepsilon_1^{\mathrm{ampl}}(N = 2)$ is plotted versus N_f (Figure 27c), the data points from the tests on samples cut either vertically or horizontally lie approximately on the same curve. This observation reveals that the cumulative effects are similar if the strain amplitude is identical for both types of sample, i.e. for the loading directions parallel or perpendicular to the sedimentation and consolidation direction.

Similar conclusions can be drawn from a comparison of the tests C24 and C42, performed with anisotropic consolidation ($\eta_0 = 0.5$) on samples cut out in different directions. The rates of axial strain accumulation $\dot{\varepsilon}_1^{\mathrm{acc}}$ are much higher in case of the conventional sample (Figure 27d), leading to a much lower number of cycles to failure (Figure 27e). The data from the tests with $\eta_0 = 0.375$ have been added in Figure 27e for orientation purpose, in order to allow a better judgement of the relationship between $q^{\mathrm{ampl}}/(2p_0)$ and N_f. However, if the strain amplitude $\varepsilon_1^{\mathrm{ampl}}(N = 2)$ is used on the ordinate instead of $q^{\mathrm{ampl}}/(2p_0)$, the data points from the samples cut out either vertically or horizontally can be approximately described by a unique curve (Figure 27f). This again confirms that the differences in the accumulation rates of horizontal and vertical samples at identical q^{ampl} are primarily due to the anisotropy of the elastic secant stiffness and the resulting different strain amplitudes in different loading directions.

4.8 Tests with strain cycles

In all tests discussed so far stress cycles have been applied. The effect of strain cycles has been examined in three additional tests (tests C43-C45 in Table 2). The normally consolidated samples ($p_0 = 300$ kPa) were subjected to a repetitive loading with constant strain amplitudes $\varepsilon_1^{\mathrm{ampl}} = 1, 2$ or 5 %. The shape of the measured effective stress paths (Figure 28) is similar to that usually observed in analo-
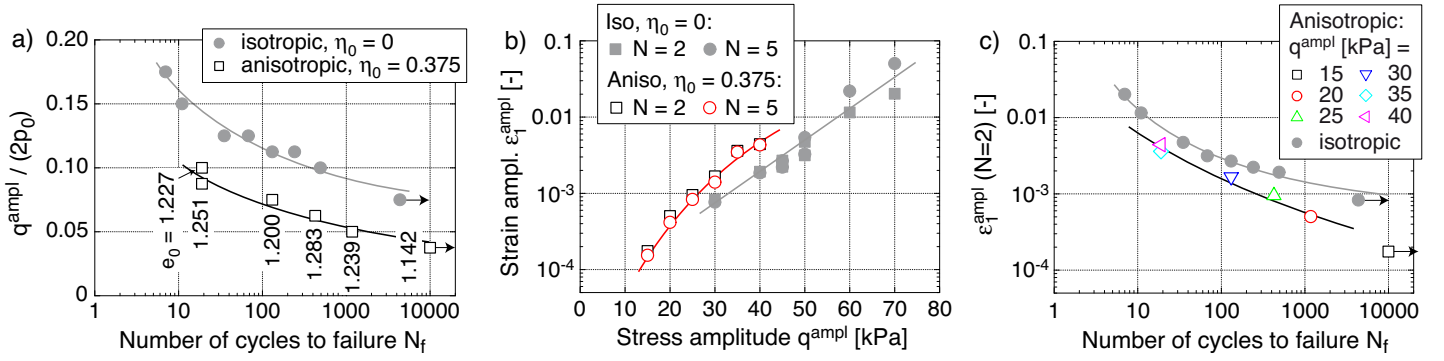
Fig. 22: *Comparison of results from test series with different stress amplitudes at either isotropic ($\eta_0 = 0$) or anisotropic ($\eta_0 = 0.375$) consolidation stresses: a) Amplitude-pressure ratio $q^{ampl}/(2p_0)$ versus number of cycles to failure N_f, b) Strain amplitude ε_1^{ampl} at $N = 2$ and $N = 5$ versus stress amplitude q^{ampl}, c) Strain amplitude $\varepsilon_1^{ampl}(N = 2)$ versus N_f*
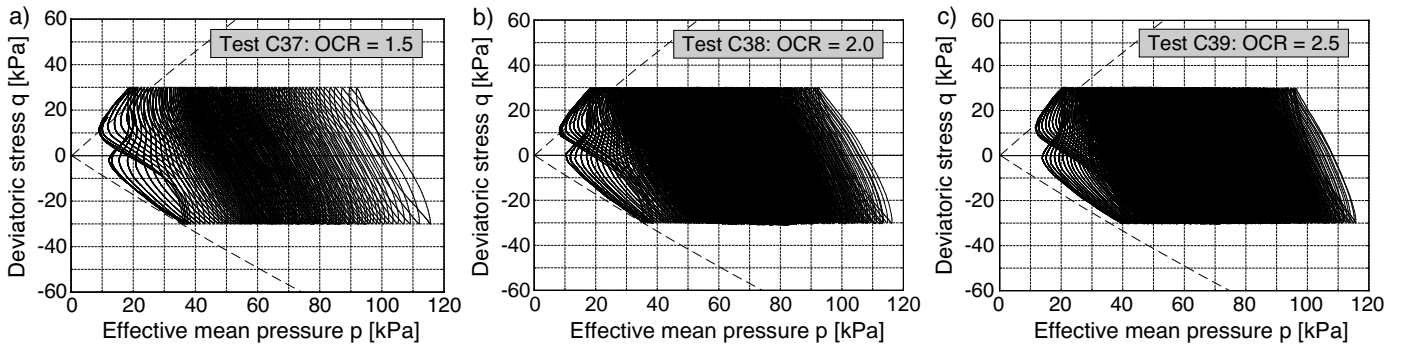

Fig. 23: *Effective stress paths in the p-q-plane measured in undrained cyclic tests performed on samples with different OCR values (all tests: $p_0 = 200$ kPa, $\eta_0 = 0.375$, $q^{ampl} = 30$ kPa, $\dot{s} = 0.1$ mm/min)*

gous tests on sand [130,131], being reminiscent of a fir tree. The p^{av}-N curve from the test with the largest strain amplitude $\varepsilon_1^{ampl} = 5$ % (Figure 29) reveals, that the average mean pressure p^{av} asymptotically reached after about 100 cycles is slightly larger than zero (about 4 kPa). This is in good agreement with [40] and in accordance with the experiments on Kaolin with stress cycles, where a state with zero effective stress has not been passed either. In the tests with both smaller strain amplitudes an asymptotic p^{av} value has not been reached within the applied number of cycles, i.e. p^{av} still shows a descending tendency at the end of a test (Figure 29).

5 Summary, conclusions and outlook

About 60 undrained monotonic or cyclic triaxial tests on Kaolin (liquid limit $w_L = 47.2$ %, plasticity index $I_P = 12.2$ %) have been performed. The samples were pre-consolidated out of a slurry. Afterwards the triaxial samples were cut out of the centre of the pre-consolidated cylinders.

The monotonic tests with different initial pressures primarily served to provide the failure lines used as reference for the analysis of the cyclic tests. Monotonic tests with different strain rates revealed a rather low rate dependence of the undrained monotonic response, which may be attributed to the low plasticity index of the tested Kaolin. Overconsolidation leads to a more dilative material behaviour and a higher undrained strength. A comparison of tests on samples cut out either vertically (conventional preparation method) or horizontally from

the pre-consolidated blocks revealed a significant effect of anisotropy: The undrained monotonic response of the horizontal samples was found more dilative and their undrained strength was higher.

In the cyclic tests the mode of failure depended on the average stress ratio η^{av}. For isotropic average stresses ($\eta^{av} = \eta_0 = 0$) the axial strain amplitude grew with increasing number of cycles and the samples finally failed due to too large strain amplitudes (a failure criterion of $|\varepsilon_1| = 10$ % was used in all tests). The effective stress paths in the final phase of such tests were eight-shaped. In contrast to typical data for sand, the effective stress path did not pass a state with zero effective stress ($p = q = 0$).

In case of anisotropic consolidation with an absolute value of the average deviatoric stress exceeding the stress amplitude ($|q^{av}| > q^{ampl}$), i.e. with stress paths completely lying in the compressional or extensional regime of the p-q plane, an accumulation of compressional or extensional axial strain with each subsequent cycle occurred. Therefore, the failure criterion was fulfilled due to an excessive accumulation of permanent strains. In contrast to the tests with isotropic consolidation, the strain amplitudes did only moderately increase during the tests. During the final phase of the tests with anisotropic consolidation the effective stress paths were lens-shaped, with the maximum (compression, $q^{av} > 0$) or minimum (extension, $q^{av} < 0$) stresses being located close to the failure lines from the monotonic tests.

In the tests with isotropic consolidation the rate of pore pressure accumulation grew with increasing stress or strain amplitude, while it was reduced with increasing values
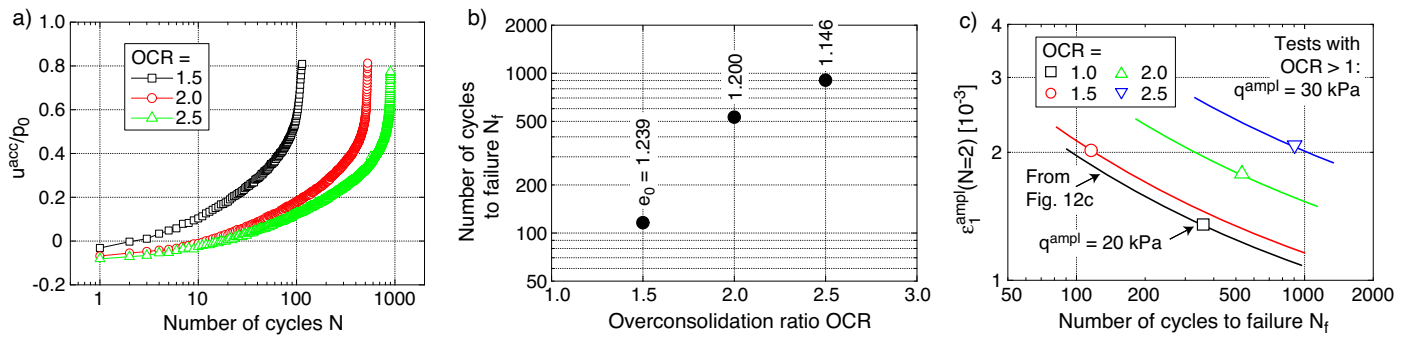
Fig. 24: *Results from tests with different overconsolidation ratios OCR: a) Normalized pore pressure accumulation curves $u^{acc}(N)/p_0$, b) number of cycles to failure N_f versus OCR, c) strain amplitude $\varepsilon_1^{ampl}(N = 2)$ versus N_f (all tests: $p_0 = 100$ kPa, $\eta_0 = 0$, $q^{ampl} = 30$ kPa, $\dot{s} = 0.1$ mm/min)*
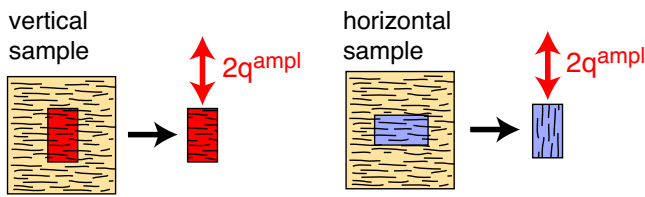

Fig. 25: *Cutting of samples from the pre-consolidated Kaolin cylinders in either the vertical or horizontal direction*

of consolidation pressure and overconsolidation ratio (at q^{ampl}/p_0 = constant). In accordance with the monotonic tests, the rate dependence of the cumulative response was found rather small. The tests with different initial stress ratios revealed a "cyclic flow rule" similar to sand: At isotropic average stresses the volumetric component of accumulation (pore pressure accumulation under undrained conditions) prevailed about the deviatoric component (accumulation of deviatoric strain). For samples cut out in the vertical direction the "cyclic flow rule" was found slightly anisotropic, i.e. a purely volumetric accumulation ($\dot{\varepsilon}_q^{acc} = 0$, $\dot{u}^{acc} \neq 0$) was observed at $\eta^{av} = 0.1$. Consequently, at $\eta^{av} = 0$ an accumulation of negative (extensional) deviatoric strains took place. With increasing absolute value of the average stress ratio $|\eta^{av}|$, the ratio between the deviatoric and volumetric portions of the accumulation rate increased. At a stress ratio corresponding to a mobilized friction angle of 19° (in both the compression and extension tests), the accumulation became purely deviatoric, i.e. the rate of pore pressure accumulation vanished while the accumulation of deviatoric strain continued ($\dot{\varepsilon}_q^{acc} \neq 0$, $\dot{u}^{acc} = 0$). Furthermore, the overall intensity of accumulation was found to increase with $|\eta^{av}|$.

Samples cut out in the horizontal direction showed an opposite inclination of the effective stress path than their vertical counterparts, for both isotropic and anisotropic consolidation stresses. Furthermore, the horizontal samples could sustain a significantly larger number of cycles to failure, which could be primarily attributed to the larger elastic stiffness and the resulting lower strain amplitudes of these samples.

Tests with strain cycles gave "fir tree"-shaped effective stress paths. As in the tests with stress amplitudes, a state with zero effective stress was also not reached in the tests with strain cycles.

The experimental database presented in this paper may serve for the development, calibration and verification of constitutive models for cohesive soils with focus to cyclic loading. All test data are available from the homepage of the first author [125].

The following aspects not considered in the present study will be a matter of future experimental research:

- Multidimensional cyclic loading, possibly involving principal stress rotations, which is known to cause larger cumulative effects compared to a one-dimensional cyclic loading [80, 113, 132].

- Soil plasticity. Usually the rates of pore pressure accumulation are lower in soils with higher plasticity indices I_P [6, 13, 37, 44, 52, 56, 96, 99].

- Pore fluid chemistry (pH value, salinity), which influences the material response via the initial fabric [36, 38–40, 85].

- Temperature effects [1, 18, 20, 25].

Acknowledgement

References

[1] H. M. Abuel-Naga, D. T. Bergado, G. V. Ramana, L. Grino, P. Rujivipat, and Y. Thet. Experimental evaluation of engineering behavior of soft Bangkok clay under elevated temperature. *Journal of Geotechnical and Geoenvironmental Engineering, ASCE*, 132(7):902–910, 2006.

[2] T. Adachi, F. Oka, T. Hirata, T. Hashimoto, J. Nagaya, M. Mimura, and T. Pradhan. Stress-strain behavior and yielding characteristics of Eastern Osaka clay. *Soils and Foundations*, 35(3):1–13, 1995.

[3] K. Akai, T. Adachi, and N. Ando. Existence of a unique stress-strain-time relation of clays. *Soils and Foundations*, 15(1):1–16, 1975.

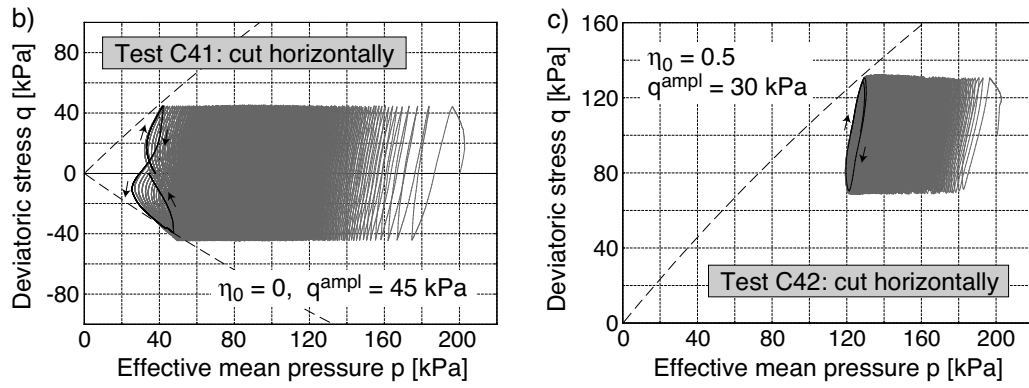[4] K.H. Andersen. Properties of soft clay under static and cyclic loading. In *NGI Publ. 176*, pages 1–20, 1988.

Fig. 26: Effective stress paths in the p-q-plane measured in undrained cyclic tests on samples cut out in the horizontal direction with a) isotropic and b) anisotropic consolidation (all tests: $p_0 = 200$ kPa, $\dot{s} = 0.1$ mm/min)
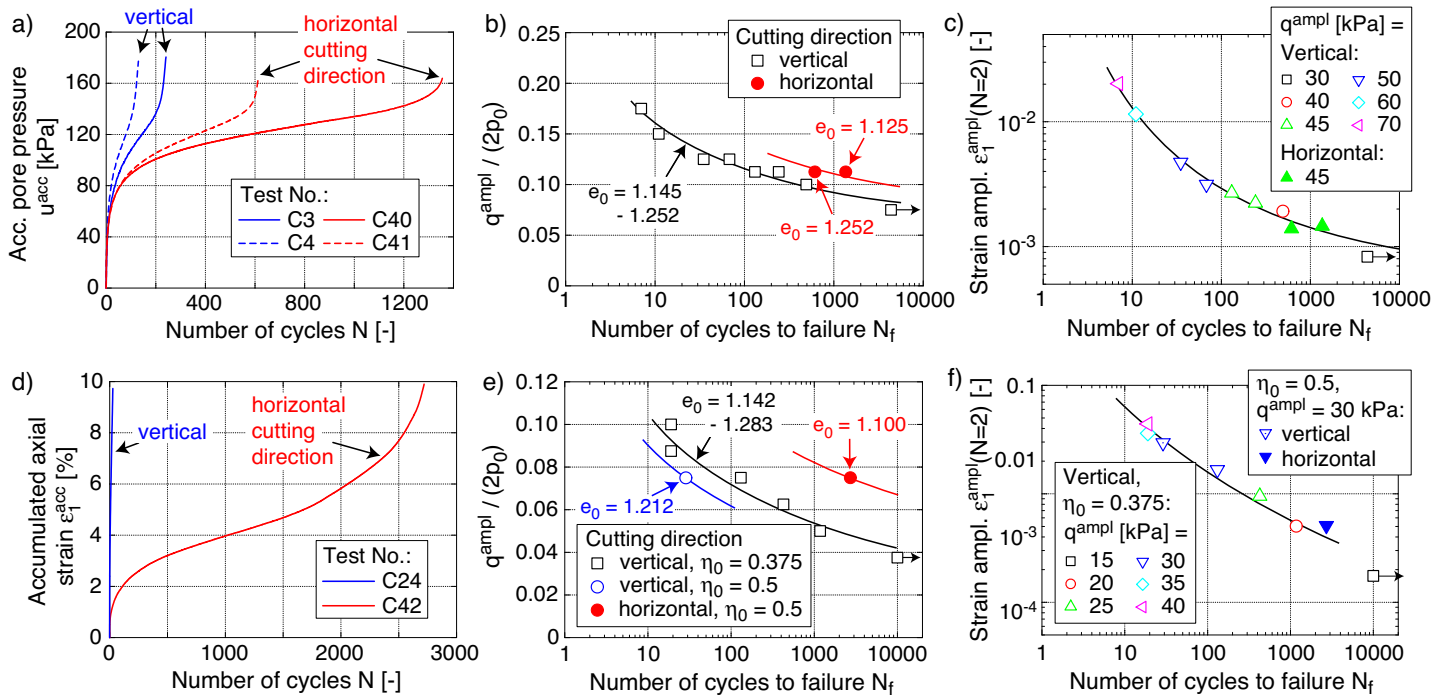

Fig. 27: Comparison of tests with samples cut out either in the horizontal or vertical direction: a,d) Accumulated pore water pressure u^{acc} or axial strain ε_1^{acc} versus number of cycles N, b,e) Amplitude-pressure ratio $q^{ampl}/(2p_0)$ versus number of cycles to failure N_f, c,f) Strain amplitude $\varepsilon_1^{ampl}(N = 2)$ versus N_f. The upper row contains data from tests with isotropic consolidation stresses ($\eta_0 = 0$), the lower row those for anisotropic ones ($\eta_0 = 0.375$ or 0.5).
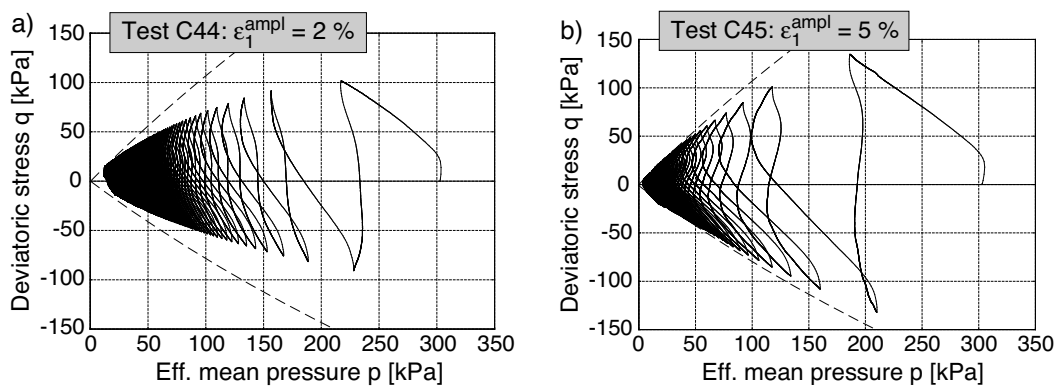

Fig. 28: Effective stress paths in the p-q-plane measured in tests with strain cycles of different amplitude (all tests: $OCR = 1$, $p_0 = 300$ kPa, $\eta_0 = 0$, $\dot{s} = 0.1$ mm/min)
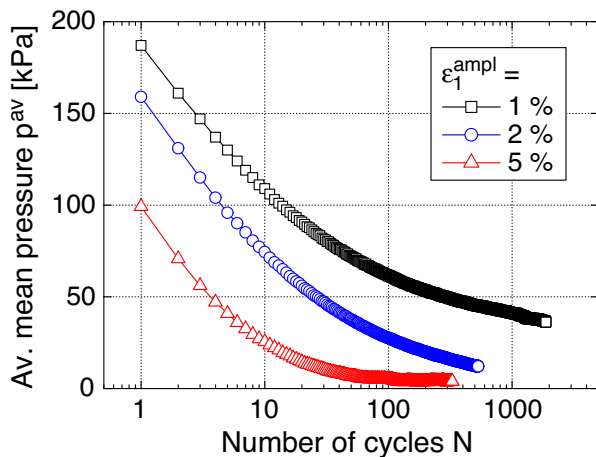
Fig. 29: *Relaxation of average mean pressure p^{av} with increasing number of cycles in tests with strain cycles of different amplitude (all tests: $OCR = 1$, $p_0 = 300$ kPa, $\eta_0 = 0$, $\dot{s} = 0.1$ mm/min)*

[5] K.H. Andersen. Cyclic clay data for foundation design of structures subjected to wave loading. In T. Triantafyllidis, editor, *Cyclic Behaviour of Soils and Liquefaction Phenomena, Proc. of CBS04, Bochum*, pages 371–387. Balkema, 31 March - 02 April 2004.

[6] K.H. Andersen. Bearing capacity under cyclic loading - offshore, along the coast, and on land. The 21st Bjerrum Lecture presented in Oslo, 23 November 2007. *Canadian Geotechnical Journal*, 46(5):513–535, 2009.

[7] K.H. Andersen, A. Kleven, and D. Heien. Cyclic soil data for design of gravity structures. *Journal of Geotechnical Engineering, ASCE*, 114(5):517–539, 1988.

[8] K.H. Andersen and R. Lauritzsen. Bearing capacity for foundations with cyclic loads. *Journal of Geotechnical Engineering, ASCE*, 114(5):540–555, 1988.

[9] K.H. Andersen, J.H. Pool, S.F. Brown, and W.F. Rosenbrand. Cyclic and static laboratory tests on Drammen clay. *Journal of the Geotechnical Engineering Division, ASCE*, 106(GT5):499–513, 1980.

[10] A. M. Ansal and A. Erken. Undrained behavior of clay under cyclic shear stresses. *Journal of Geotechnical Engineering, ASCE*, 115(7):968–983, 1989.

[11] J. Atkinson. Peak strength of overconsolidated clays. *Géotechnique*, 57(2):127–135, 2007.

[12] A.S. Azzouz, A.M. Malek, and M.B. Mohsen. Cyclic behavior of clays in undrained simple shear. *Journal of Geotechnical Engineering, ASCE*, 115(5):637–657, 1989.

[13] R.W. Boulanger and I.M. Idriss. Liquefaction susceptibility criteria for silts and clays. *Journal of Geotechnical and Geoenvironmental Engineering, ASCE*, 132(11):1413–1428, 2006.

[14] R.W. Boulanger and I.M. Idriss. Evaluation of cyclic softening in silts and clays. *Soils and Foundations*, 133(6):641–652, 2007.

[15] R.W. Boulanger, M.W. Meyers, L.H. Mejia, and I.M. Idriss. Behavior of a fine-grained soil during the Loma Prieta earthquake. *Canadian Geotechnical Journal*, 35(1):146–158, 1998.

[16] S.F. Brown, A.K.F. Lashine, and A.F.L Hyde. Repeated load triaxial testing of a silty clay. *Géotechnique*, 25(1):95–114, 1975.

[17] Y. Cai, C. Gu, J. Wang, C. H. Juang, C. Xu, and Hu. X. One-way cyclic triaxial behavior of saturated clay: Comparison between constant and variable confining pressure. *Journal of Geotechnical and Geoenvironmental Engineering, ASCE*, 139(5):797–809, 2013.

[18] R.D. Campanella and J.K. Mitchell. Influence of temperature variations on soil behavior. *Journal of the Soil Mechanics and Foundations Division, ASCE*, 94(SM3):709–734, 1968.

[19] B. Casey and J. T. Germaine. Stress dependence of shear strength in fine-grained soils and correlations with liquid limit. *Journal of Geotechnical and Geoenvironmental Engineering, ASCE*, 139(10):1709–1717, 2013.

[20] C. Cekerevac and L. Laloui. Experimental analysis of the cyclic behaviour of kaolin at high temperature. *Géotechnique*, 60(8):651–655, 2010.

[21] J. Choo, Y.-H. Jung, W. Cho, and C.-K. Chung. Effect of pre-shear stress path on nonlinear shear stiffness degradation of cohesive soils. *Geotechnical Testing Journal, ASTM*, 36(2):1–8, 2013.

[22] J. Choo, Y.-H. Jung, and C.-K. Chung. Effect of directional stress history on anisotropy of initial stiffness of cohesive soils measured by bender element tests. *Soils and Foundations*, 51(4):737–747, 2011.

[23] D.B. Chu, J.P. Stewart, R.W. Boulanger, and P.S. Lin. Cyclic softening of low-plasticity clay and its effect on seismic foundation performance. *Journal of Geotechnical and Geoenvironmental Engineering, ASCE*, 134(11):1595–1608, 2008.

[24] H. Chu and M Vucetic. Settlement of campacted clay in a cyclic direct simple shear device. *Geotechnical Testing Journal, ASTM*, 15(4):371–379, 1992.

[25] K.R. Demars and R.D. Charles. Soil volume changes induced by temperature cycling. *Canadian Geotechnical Journal*, 19:188–194, 1982.

[26] J.A. Díaz-Rodríguez, J.J. Martinez-Vasquez, and J.C. Santamarina. Strain-rate effects in Mexico City soil. *Journal of Geotechnical and Geoenvironmental Engineering, ASCE*, 135(2):300–305, 2009.

[27] A. d'Onofrio, F. Silvestri, and F. Vinale. Strain rate dependent behaviour of a natural stiff clay. *Soils and Foundations*, 39(2):69–82, 1999.

[28] J. M. Duncan and H. B. Seed. Anisotropy and stress reorientation in clay. *Journal of the Soil Mechanics and Foundations Division, ASCE*, 92(SM5):21–52, 1966.

[29] R. J. Finno and C. K. Chung. Stress-strain-strength responses of compressible Chicago glacial clays. *Journal of Geotechnical Engineering, ASCE*, 118(10):1607–1625, 1992.

[30] M.W. Frost, P.R. Fleming, and C.D.F. Rogers. Cyclic triaxial tests on clay subgrades for analytical pavement design. *Journal of Testing and Evaluation*, 130(3):378–386, 2004.

[31] A. Gasparre, D.W. Hight, M.R. Coop, and R.J. Jardine. The laboratory measurement and interpretation of the small-strain stiffness of stiff clays. *Géotechnique*, 64(12):942–953, 2014.

[32] A. Gasparre, S. Nishimura, M.R. Coop, and R.J. Jardine. The influence of structure on the behavior of London Clay. *Géotechnique*, 57(1):19–31, 2007.

[33] A. Gasparre, S. Nishimura, N. A. Minh, M. R. Coop, and R. J. Jardine. The stiffness of natural London clay. *Géotechnique*, 57(1):33–47, 2007.

[34] A.M. Goulois, R.V. Whitman, and K. Hoeg. Effects of sustained shear stresses on the cyclic degradation of clay. In R.C. Chaney and K.R. Demars, editors, *Strength testing of marine sediments; ASTM STP 883*, pages 336–351. ASTM, Philadelphia, 1985.

[35] G. Graham, J.H.A. Crooks, and A.L. Bell. Time effects on the stress-strain behaviour of soft natural clays. *Géotechnique*, 33(3):327–340, 1983.

[36] I. Gratchev, K. Sassa, V. Osipov, H. Fukuoka, and G. Wang. Undrained cyclic behavior of bentonite-sand mixtures and factors affecting it. *Geotechnical and Geological Engineering*, 25(3):349–367, 2007.

[37] I. Gratchev, K. Sassa, V. Osipov, and V. Sokolov. The liquefaction of clayey soils under cyclic loading. *Engineering Geology*, 86(1):70–84, 2006.

[38] I. B. Gratchev and K. Sassa. Cyclic shear strength of soil with different pore fluids. *Journal of Geotechnical and Geoenvironmental Engineering, ASCE*, 139(10):1817–1821, 2013.

[39] I. B. Gratchev, K. Sassa, and H. Fukuoka. How Reliable is the plasticity index for estimating the liquefaction potential of clayey sands? *Journal of Geotechnical and Geoenvironmental Engineering, ASCE*, 132(1):124–127, 2006.

[40] I.B. Gratchev and K. Sassa. Cyclic behavior of fine-grained soils at different pH values. *Journal of Geotechnical and Geoenvironmental Engineering, ASCE*, 135(2):271–279, 2009.

[41] C. Gu, J. Wang, Y. Cai, and L. Guo. Influence of cyclic loading history on small strain shear modulus of saturated clays. *Soil Dynamics and Earthquake Engineering*, 66:1–12, 2014.

[42] C. Gu, J. Wang, Y. Cai, Z. Yang, and Y. Gao. Undrained cyclic triaxial behavior of saturated clays under variable confining pressure. *Soil Dynamics and Earthquake Engineering*, 40:118–128, 2012.

[43] L. Guo, J. Wang, Y. Cai, H. Lui, Y. Gao, and H. Sun. Undrained deformation behavior of saturated soft clay under long-term cyclic loading. *Soil Dynamics and Earthquake Engineering*, 50:28–37, 2013.

[44] T. Guo and S. Prakash. Liquefaction of silt and silt-clay mixtures. *Journal of Geotechnical and Geoenvironmental Engineering, ASCE*, 125(8):706–710, 1999.

[45] A.S. Gylland and H.P. Jostad. Experimental study of strain localization in sensitive clays. *Acta Geotechnica*, 9:227–240, 2014.

[46] A.M. Hanna and K. Javed. Experimental investigation of foundations on sensitive clay subjected to cyclic loading. *Journal of Geotechnical and Geoenvironmental Engineering, ASCE*, pages 04014065–1 – 04014065–12, 2014.

[47] P.-Y. Hicher, H. Wahyudi, and D. Tessier. Microstructural analysis of inherent and induced anisotropy in clay. *Mechanics of Cohesive-Frictional Materials*, 5(5):341–371, 2000.

[48] D.W. Hight, A.J. Bond, and J.D. Legge. Characterization of the Bothkennar clay: an overview. *Géotechnique*, 42(2):303–347, 1992.

[49] C.-C. Hsu and M. Vucetic. Volumetric threshold shear strain for cyclic settlement. *Journal of Geotechnical and Geoenvironmental Engineering, ASCE*, 132(1):58–70, 2004.

[50] C.-C. Hsu and M. Vucetic. Threshold shear strain for cyclic pore-water pressure in cohesive soils. *Journal of Geotechnical and Geoenvironmental Engineering, ASCE*, 132(10):1325–1335, 2006.

[51] A.F.L. Hyde, K. Yasuhara, and K. Hirao. Stability criteria for marine clay under one-way cyclic loading. *Journal of Geotechnical Engineering, ASCE*, 119(11):1771–1789, 1993.

[52] M. Hyodo, A.F.L. Hyde, Y. Yamamoto, and T. Fujii. Cyclic shear strength of undisturbed and remoulded marine clays. *Soils and Foundations*, 39(2):45–58, 1999.

[53] M. Hyodo, Y. Yamamoto, and M. Sugiyama. Undrained cyclic shear behaviour of normally consolidated clay subjected to initial static shear stress. *Soils and Foundations*, 34(4):1–11, 1994.

[54] M. Hyodo, K. Yasuhara, and K. Hirao. Prediction of clay behavior in undrained and partially drained cyclic triaxial tests. *Soils and Foundations*, 32(4):117–127, 1992.

[55] I. Ishibashi and X. Zhang. Unified dynamic shear moduli and damping ratios of sand and clay. *Soils and Foundations*, 33(1):182–191, 1993.

[56] K. Ishihara, J. Troncoso, Y. Kawase, and Y. Takahashi. Cyclic strength characteristics of tailings materials. *Soils and Foundations*, 20:127–142, 1980.

[57] T. Kawaguchi and H. Tanaka. Formulation of $G_{\max}$ from reconstituted clayey soils and its application to $G_{\max}$ measured in the field. *Soils and Foundations*, 48(6):821–831, 2008.

[58] T.C. Kim and M. Novak. Dynamic properties of some cohesive soils of Ontario. *Canadian Geotechnical Journal*, 18:371–389, 1981.

[59] T. Kokusho, Y. Yoshida, and Y. Esashi. Dynamic properties of soft clays for wide strain range. *Soils and Foundations*, 22(4):1–18, 1982.

[60] D. Koutsoftas and J. Fischer. Dynamic properties of two marine clays. *Journal of the Geotechnical Engineering Division, ASCE*, 106(GT6):645–657, 1980.

[61] C. C. Ladd. Stability evaluation during staged construction. *Journal of Geotechnical Engineering, ASCE*, 117(4):540–615, 1991.

[62] C.C. Ladd and R. Foott. New design procedure for stability of soft clays. *Journal of the Geotechnical Engineering Division, ASCE*, 100(GT7):763–786, 1974.

[63] G. Lanzo, A. Pagliaroli, P. Tommasi, and F.L. Chiocci. Simple shear testing of sensitive, very soft offshore clay for wide strain range. *Canadian Geotechnical Journal*, 46(11):1277–1288, 2009.

[64] A.K. Lashine. *Some aspects of the characteristics of Keuper marl under repeated loading*. PhD thesis, University of Nottingham, 1971.

[65] C.-J. Lee and S.-F. Sheu. The stiffness degradation and damping ratio evolution of Taipei Silty Clay under cyclic straining. *Soil Dynamics and Earthquake Engineering*, 27(8):730–740, 2007.

[66] G. Lefebvre and D. LeBoeuf. Rate effects and cyclic loading of sensitive clays. *Journal of Geotechnical Engineering, ASCE*, 113(5):476–489, 1987.

[67] G. Lefebvre and P. Pfendler. Strain rate and preshear effects in cyclic resistance of soft clay. *Journal of Geotechnical Engineering, ASCE*, 122(1):21–26, 1996.

[68] D. Li and E.T. Selig. Cumulative plastic deformation for fine-grained subgrade soils. *Journal of Geotechnical Engineering, ASCE*, 122(12):1006–1013, 1996.

[69] L.L. Li, H.B. Dan, and L.Z. Wang. Undrained behavior of natural marine clay under cyclic loading. *Ocean Engineering*, 38:1792–1805, 2011.

[70] S. Likitlersuang, S. Teachavorasinskun, C. Surarak, E. Oh, and A. Balasubramaniam. Small strain stiffness and stiffness degradation curve of Bangkok clays. *Soils and Foundations*, 53(4):498–509, 2013.

[71] K. Y. Lo and J. P. Morin. Strength anisotropy and time effects of two sensitive clays. *Canadian Geotechnical Journal*, 9(3):261–277, 1972.

[72] K.Y. Lo. Stability of slopes in anisotropic soils. *Journal of the Soil Mechanics and Foundations Division, ASCE*, 91(SM4):85–106, 1965.

[73] T. Lunne, T. Berre, K.H. Andersen, S. Strandvik, and M. Sjursen. Effects of sample disturbance and consolidation procedures on measured shear strength of soft marine Norwegian clays. *Canadian Geotechnical Journal*, 43:726–750, 2006.

[74] T.A. Macky and A.S. Saada. Dynamics of anisotropic clays under large strains. *Journal of Geotechnical Engineering, ASCE*, 110(4):487–504, 1984.

[75] A.M. Malek. *Cyclic behavior of clay in undrained simple shearing and application to offshore tension piles*. PhD thesis, Massachusetts Institute of Technology (MIT), June 1987.

[76] A.M. Malek, A.S. Azzouz, M.M. Baligh, and J.T. Germaine. Behavior of foundation clays supporting compliant offshore structures. *Journal of Geotechnical Engineering, ASCE*, 115(5):615–635, 1989.

[77] M. Matasovic, N. Vucetic. A pore pressure model for cyclic straining of clay. *Soils and Foundations*, 32(3):156–173, 1992.

[78] N. Matasovic and M. Vucetic. Generalized cyclic-degradation-pore-pressure generation model for clays. *Journal of Geotechnical Engineering, ASCE*, 121(1):33–42, 1995.

[79] L. Matešic and M. Vucetic. Strain-rate effect on soil secant shear modulus at small cyclic strains. *Journal of Geotechnical and Geoenvironmental Engineering, ASCE*, 129(6):536–549, 2003.

[80] H. Matsuda, T. T. Nhan, and R. Ishikura. Prediction of excess pore water pressure and post-cyclic settlement on soft clay induced by uni-directional and multi-directional cyclic shears as a function of strain path parameters. *Soil Dynamics and Earthquake Engineering*, 49:75–88, 2013.

[81] T. Matsui, H. Ohara, and T. Ito. Cyclic stress-strain history and shear characteristics of clay. *Journal of the Geotechnical Engineering Division, ASCE*, 106(GT10):1101–1120, 1980.

[82] R. J. Mitchell. On the yielding and mechanical strength of Leda clays. *Canadian Geotechnical Journal*, 7:297–312, 1970.

[83] R.J. Mitchell and P.K.K. Wong. The generalized failure of an Ottawa Valley Champlain clay. *Canadian Geotechnical Journal*, 10:607–616, 1973.

[84] A.R. Mortezaie and M. Vucetic. Effect of frequency and vertical stress on cyclic degradation and pore water pressure in clay in the NGI simple shear device. *Journal of Geotechnical and Geoenvironmental Engineering, ASCE*, 139(10):1727–1737, 2013.

[85] H. Nagase, K. Shimizu, A. Hiro-oka, Y. Tanoue, and Y. Saitoh. Earthquake-induced residual deformation of Ariake clay deposits with leaching. *Soil Dynamics and Earthquake Engineering*, 26(2-4):209–220, 2006.

[86] C.W.W. Ng, G.B. Liu, and Q. Li. Investigation of the long-term tunnel settlement mechanisms of the first metro line in Shanghai. *Canadian Geotechnical Journal*, 50(6):674–684, 2013.

[87] A. Niemunis, T. Wichtmann, and Th. Triantafyllidis. A high-cycle accumulation model for sand. *Computers and Geotechnics*, 32(4):245–263, 2005.

[88] S. Ohara and H. Matsuda. Study on the settlement of saturated clay layer induced by cyclic shear. *Soils and Foundations*, 28(3):103–113, 1988.

[89] D.V. Okur and A. Ansal. Stiffness degradation of natural fine grained soils during cyclic loading. *Soil Dynamics and Earthquake Engineering*, 27(9):843–854, 2007.

[90] M.P. O'Reilly, S.F. Brown, and R.F. Overy. Viscous effects observed in tests on an anisotropically normally consolidated silty clay. *Géotechnique*, 39(1):153–158, 1989.

[91] R.H.G. Parry. Triaxial compression and extension tests on remoulded saturated clay. *Géotechnique*, 10:166–180, 1960.

[92] H. Patiño, A. Soriano, and J. González. Failure of a soft cohesive soil subjected to combined static and cyclic loading. *Soils and Foundations*, 53(6):910–922, 2013.

[93] D.S. Pennington, D.F.T. Nash, and M.L. Lings. Anisotropy of G_0 shear stiffness in Gault clay. *Géotechnique*, 47(3):391–398, 1997.

[94] D. Penumadu, A. Skandarajah, and J.-L. Chameau. Strain rate effects in pressuremeter testing using a cuboidal shear device: experiments and modeling. *Canadian Geotechnical Journal*, (35):27–42, 1998.

[95] D. C Procter and J. Khaffaf. Cyclic triaxial tests on remolded clays. *Journal of Geotechnical Engineering, ASCE*, 110(10):1431–1445, 1984.

[96] V.K. Puri. *Liquefaction behavior and dynamic properties of loessial (silty) soils*. PhD thesis, University of Missouri-Rollo, 1984.

[97] S. Rampello and L. Callisto. A study on the subsoil of the Tower of Pisa based on results from standard and high-quality samples. *Canadian Geotechnical Journal*, 35(6):1074–1092, 1998.

[98] W. Ratananikom, S. Likitlersuang, and S. Yimsiri. An investigation of anisotropic elastic parameters of Bangkok clay from vertical and horizontal cut specimens. *Geomechanics and Geoengineering: An International Journal*, 8(1):15–27, 2012.

[99] S. Romero. The behavior of silt as clay content is increased. Master's thesis, University of California, Davis, California, 1995.

[100] K.H. Roscoe, A.N. Schofield, and C.P. Wroth. On the yielding of soils. *Géotechnique*, 8(1):22–53, 1958.

[101] Shibuya S., T. Mitachi, F. Fukuda, and T. Degoshi. Strain rate effects on shear modulus and damping of normally consolidated clay. *Geotechnical Testing Journal, ASTM*, 18(3):365–375, 1995.

[102] A. Saada, G. Bianchini, and L. Liang. Cracks, bifurcation and shear band propagation in saturated clays. *Géotechnique*, 44(1):35–64, 1994.

[103] A. Sakai, L. Samang, and N. Miura. Partially-drained cyclic behavior and its application to the settlement of a low embankment road on silty-clay. *Soils and Foundations*, 43(1):33–46, 2003.

[104] M. Santagata, J.T. Germaine, and C.C. Ladd. Small-strain nonlinearity of normally consolidated clay. *Journal of Geotechnical and Geoenvironmental Engineering, ASCE*, 133(1):72–82, 2007.

[105] H.B. Seed and C.K. Chan. Clay strength under earthquake loading conditions. *Journal of the Soil Mechanics and Foundations Division, ASCE*, 92(SM2):53–78, 1966.

[106] S. Seng and H. Tanaka. Properties of very soft clays: A study of thixotropic hardening and behavior under low consolidation pressure. *Soils and Foundations*, 52(2):335–345, 2012.

[107] T. C. Sheahan, C. C. Ladd, and J. T. Germaine. Rate dependent undrained shear behavior of saturated clay. *Journal of Geotechnical Engineering, ASCE*, 122(2):99–108, 1996.

[108] S. Shibuya and T. Mitachi. Small strain modulus of clay sedimentation in a state of normal consolidation. *Soils and Foundations*, 34(4):67–77, 1994.

[109] T. Shogaki and N. Kumagai. A slope stability analysis considering undrained strength anisotropy of natural clay deposits. *Soils and Foundations*, 48(6):805–819, 2008.

[110] V. Sivakumar, I.G. Doran, and J. Graham. Particle orientation and its influence on the mechanical behavior of isotropically consolidated reconstituted clay. *Engineering Geology*, 66:197–209, 2002.

[111] K. K. Sorensen, B. A. Baudet, and B. Simpson. Influence of structure on the time-dependent behaviour of a stiff sedimentary clay. *Géotechnique*, 57(1):113–124, 2007.

[112] K.H. Stokoe, M.B. Darendeli, R.D. Andrus, and L.T. Brown. Dynamic soil properties: laboratory, field and correlation studies. In *Proc. 2nd Int. Conf. on Earthquake Geotech. Eng.*, volume 3, pages 811–845. A.A. Balkema, 1999.

[113] D. Su, W.L. Wu, Z.Y. Du, and W.M. Yan. Cyclic degradation of a multidirectionally laterally loaded rigid single pile model in compacted clay. *Journal of Geotechnical and Geoenvironmental Engineering, ASCE*, 140(5):06014002–1–06014002–7, 2014.

[114] Y.-Q. Tang, J. Zhou, S. Liu, P. Yang, and J.-X. Wang. Test on cyclic creep behavior of mucky clay in Shanghai under step cyclic loading. *EES*, 63:321–327, 2011.

[115] S. Teachavorasinskun, P. Thongchim, and Lukkunaprasit. P. Shear modulus and damping of soft Bangkog clays. *Canadian Geotechnical Journal*, 39(5):1201–1208, 2002.

[116] Y.P. Vaid and R.G. Campanella. Time dependent behavior of undisturbed clay. *Journal of Geotechnical Engineering, ASCE*, 103(7):693–709, 1977.

[117] Y.P. Vaid, P.K. Robertson, and R.G. Campanella. Strain rate behaviour of the Saint-Jean-Vianney clay. *Canadian Geotechnical Journal*, 16(1):34–42, 1979.

[118] H.A.M. Van Eekelen and D.M. Potts. The behavior of Drammen clay under cyclic loading. *Géotechnique*, 28(2):173–196, 1978.

[119] P.J. Vardanega and M.D. Bolton. Stiffness of clays and silts: normalizing shear modulus and shear strain. *Journal of Geotechnical and Geoenvironmental Engineering, ASCE*, 139(9):1575–1589, 2013.

[120] P.J. Vardanega and M.D. Bolton. Stiffness of clays and silts: modeling considerations. *Journal of Geotechnical and Geoenvironmental Engineering, ASCE*, 140(6):06014004–1–06014004–7, 2014.

[121] G. Viggiani and J.H. Atkinson. Stiffness of fine-grained soil at very small strains. *Géotechnique*, 45(2):249–265, 1995.

[122] E.A. Voznesensky and S. Nordal. Dynamic instability of clays: an energy approach. *Soil Dynamics and Earthquake Engineering*, 18:125–133, 1999.

[123] M. Vucetic. Normalized behavior of offshore clay under uniform cyclic loading. *Canadian Geotechnical Journal*, 25:33–41, 1988.

[124] M. Vucetic. Cyclic threshold shear strains in soils. *Journal of Geotechnical Engineering, ASCE*, 120(12):2208–2228, 1994.

[125] T. Wichtmann. www.torsten-wichtmann.de. Homepage, 2018.

[126] T. Wichtmann, K.H. Andersen, M.A. Sjursen, and T. Berre. Cyclic behaviour of high-quality undisturbed block samples of Onsøy clay. *Canadian Geotechnical Journal*, 50(4):400–412, 2013.

[127] T. Wichtmann, A. Niemunis, and Th. Triantafyllidis. On the "elastic stiffness" in a high-cycle accumulation model - continued investigations. *Canadian Geotechnical Journal*, 50(12):1260–1272, 2013.

[128] T. Wichtmann, A. Niemunis, and Th. Triantafyllidis. Flow rule in a high-cycle accumulation model backed by cyclic test data of 22 sands. *Acta Geotechnica*, 9(4):695–709, 2014.

[129] T. Wichtmann, H.A. Rondón, A. Niemunis, Th. Triantafyllidis, and A. Lizcano. Prediction of permanent deformations in pavements using a high-cycle accumulation model. *Journal of Geotechnical and Geoenvironmental Engineering, ASCE*, 136(5):728–740, 2010.

[130] T. Wichtmann and Th. Triantafyllidis. An experimental data base for the development, calibration and verification of constitutive models for sand with focus to cyclic loading. Part I: Tests with monotonic loading and stress cycles. *Acta Geotechnica*, 11(4):739–761, 2016.

[131] T. Wichtmann and Th. Triantafyllidis. An experimental data base for the development, calibration and verification of constitutive models for sand with focus to cyclic loading. Part II: tests with strain cycles and combined cyclic and monotonic loading. *Acta Geotechnica*, 11(4):763–774, 2016.

[132] J. Xiao, C. H. Juang, K. Wei, and Xu. S. Effects of principal stress rotation on the cumulative deformation of normally consolidated soft clay under subway traffic loading. *Journal of Geotechnical and Geoenvironmental Engineering, ASCE*, 140(4):04013046–1 − 04013046–9, 2014.

[133] K. Yasuhara, K. Hirao, and A. Hyde. Effects of cyclic loading on undrained strength and compressibility of clay. *Soils and Foundations*, 32(1):100–116, 1992.

[134] K. Yasuhara, T. Yamanouchi, and K. Hirao. Cyclic strength and deformation of normally consolidated clay. *Soils and Foundations*, 22(3):77–91, 1982.

[135] S. Yimsiri and K. Soga. Cross-anisotropic elastic parameters of two natural stiff clays. *Géotechnique*, 61(9):809–814, 2011.

[136] M. Zergoun and Y.P. Vaid. Effective stress response of clay to undrained cyclic loading. *Canadian Geotechnical Journal*, 31:714–727, 1994.

[137] J. Zhou and X. Gong. Strain degradation of saturated clay under cyclic loading. *Canadian Geotechnical Journal*, 38:208–212, 2001.

[138] T.F. Zimmie and C.Y. Lien. Response of clay subjected to combined cyclic and initial static shear stress. In *Proc. 3rd Can. Conf. on Marine Geotech. Egnrg.*, volume 2, pages 655–675, 1986.

Appendix: Generalized flow rule considering anisotropy

The equations for the generalized flow rule applied in Section 4.4 are briefly outlined in the following. The generalized flow rule has been proposed in [129] as a component

of the high-cycle accumulation (HCA) model of Niemunis et al. [87]. It allows for considering anisotropy. The equations do not distinguish between an inherent and an induced anisotropy. A second-order anisotropy tensor

$$\mathbf{a} = \boldsymbol{\sigma}^*/p \qquad (4)$$

is introduced with $\boldsymbol{\sigma}$ being a stress for which the flow rule is assumed purely volumetric, $\mathbf{m}(\mathbf{a}) = \vec{\mathbf{1}}$. The deviatoric part of $\boldsymbol{\sigma}$ is denoted as $\boldsymbol{\sigma}^*$. The isotropic flow rule can be recovered by setting $\mathbf{a} = \mathbf{0}$. For the critical state the flow rule is purely deviatoric. For an intermediate stress $\boldsymbol{\sigma}$ an interpolation is used. Given $\mathbf{a}$, the stress $\boldsymbol{\sigma}$ is projected radially onto the deviatoric plane expressed by $p = 1$. Next, the projected stress $\boldsymbol{\sigma}/p$ is decomposed as follows (Figure 30a):

$$\boldsymbol{\sigma}/p = \mathbf{1} + \mathbf{r} = \mathbf{1} + \boldsymbol{\sigma}^*/p \qquad (5)$$

The conjugated stress $\mathbf{t}$ is found from

$$\mathbf{t} = \mathbf{1} + \mathbf{a} + \lambda(\mathbf{r} - \mathbf{a}) \qquad (6)$$

It should lie on the critical surface at $p = 1$ (Figure 30b). For that purpose the scalar multiplier λ must be determined from the condition that the conjugated stress $\mathbf{t}$ satisfies

$$\operatorname{tr} \mathbf{t} \, \operatorname{tr}\left(\mathbf{t}^{-1}\right) = Y_c \qquad \text{or} \qquad \operatorname{tr}\left(\mathbf{t}^{-1}\right) = -Y_c/3 \qquad (7)$$

with Y_c calculated from:

$$Y_c = \frac{9 - \sin^2 \varphi_{cc}}{1 - \sin^2 \varphi_{cc}} \qquad (8)$$

Therein φ_{cc} is a material constant being similar (but not necessarily identical) to the critical friction angle φ_c. Having found λ the generalized flow rule is calculated from

$$\mathbf{m} = \frac{1}{\sqrt{(1 - \lambda^{-n})^2 + (\lambda^{-n})^2}} \left[\vec{\mathbf{1}}(1 - \lambda^{-n}) + \lambda^{-n}(\mathbf{t}^*)^{\rightarrow}\right] \quad (9)$$

wherein n is an interpolation parameter (another material constant). Linear interpolation is obtained with $n = 1$.
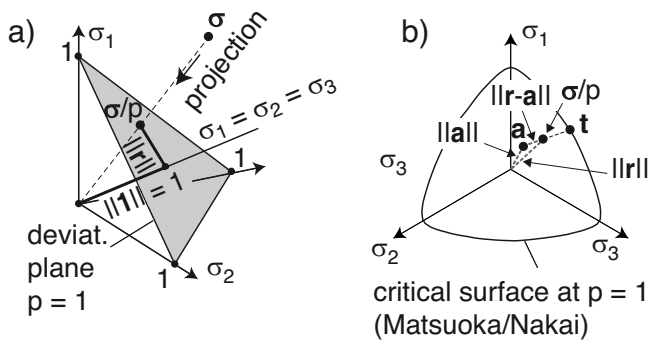

Fig. 30: *a) Projection of stress $\boldsymbol{\sigma}$ on the surface $p = 1$, b) Determination of the conjugated stress $\mathbf{t}$*

As an example, the flow rule $\mathbf{m}$ for the axisymmetric stress state in a triaxial test with the diagonal components

$$\boldsymbol{\sigma} = \operatorname{diag}(\sigma_1, \sigma_3, \sigma_3) \qquad (10)$$

and for a transversal isotropy

$$\mathbf{a} = \operatorname{diag}(a, -a/2, -a/2). \qquad (11)$$

is derived. The parameter a and the stress ratio η_{iso} for which the accumulation is purely volumetric are interrelated via

$$a = -2/3 \, \eta_{\text{iso}}. \qquad (12)$$

Furthermore,

$$\mathbf{r} = \operatorname{diag}(r, -r/2, -r/2) \quad \text{with} \quad r = -2/3 \, \eta \quad (13)$$

holds. From two solutions of Eq. (7)

$$\begin{aligned}
\lambda_{1|2} = \quad & \frac{1}{2(a - r)^2 Y_c}\Big[-9a \\
& + 3\left(3r \pm \sqrt{(a - r)^2(Y_c - 9)(Y_c - 1)}\right) \\
& + (2a + 1)(a - r)Y_c\Big]
\end{aligned} \qquad (14)$$

the positive one is chosen as λ. Finally, the strain rate ratio $\omega = \dot{\varepsilon}_v^{\text{acc}}/\dot{\varepsilon}_q^{\text{acc}}$ shown in Figure 19 is calculated from

$$\omega = \frac{1 - \lambda^{-n}}{\lambda^{-n}} \quad \text{or} \quad \omega = -\frac{1 - \lambda^{-n}}{\lambda^{-n}} \qquad (15)$$

for triaxial compression or extension, respectively.